The Mousny massive quartz occurrence – the vestige of a late-orogenic dilational jog in the High-Ardenne slate belt (Belgium)

Simon DEPOORTER[1, 3], Dominique JACQUES[1], Kris PIESSENS[2], Philippe MUCHEZ[1] & Manuel SINTUBIN[1*]

[1] Geodynamics and Geofluids Research Group, Department of Earth and Environmental Sciences, KU Leuven, Celestijnenlaan 200E, B-3001 Leuven, Belgium
[2] Geological Survey of Belgium, Royal Belgian Institute of Natural Sciences, Jennerstraat 13, B-1000 Brussels, Belgium
[3] now at GEOS constructive testing, Hertenstraat 30, B-3830 Wellen, Belgium
* corresponding author: manuel.sintubin@ees.kuleuven.be

ABSTRACT. Near the village of Mousny, Belgium, a peculiar massive quartz occurrence, composed of multiple large, >m³-size, bodies of milky quartz can be found at the locality known as *"Les Blancs Cailloux"*. Strikingly, the quartz bodies contain elongated, cleaved, host-rock fragments, still oriented parallel to the regional cleavage attitude.

A detailed petrographical, microstructural and mineralogical study of the vein quartz and a geochemical analysis of fluid inclusions has revealed that the Mousny massive quartz occurrence is genetically linked to the regionally common cleavage-parallel quartz veins. They both show a fluid evolution typical of the metamorphic fluids in the central, epizonal part of the High-Ardenne slate belt.

While the cleavage-parallel veins can be considered to result from mode I extensional fracturing, the genetically linked massive quartz occurrence is seen as being formed in a dilational jog. Within the late-orogenic context of the High-Ardenne slate belt, we favour a model in which the dilational jog is comprised within a weakly south-dipping, extensional shear zone, related to the late-orogenic extensional destabilization of the slate belt, causing a transient enhancement of the structural permeability in this low-permeability mid-crustal environment. The Mousny massive quartz occurrence may in this respect be exemplary for massive quartz occurrences throughout the High-Ardenne slate belt.

KEYWORDS: Microthermometry, Raman microspectroscopy, Variscan orogeny, fluid inclusion, optical microscopy, cathodoluminescence, tectonic inversion, orogenic collapse

1. Introduction

In low-permeability, mid-crustal environments, such as slate belts, generating and maintaining transient structural permeability is of paramount importance for fluid redistribution and subsequent ore genesis (e.g. Cox, 2005; Sibson, 2004; Upton et al., 2011). The widespread quartz-vein occurrence in the High-Ardenne slate belt (HASB) (Belgium, Germany, France) has proven an ideal proxy to reconstruct the coupled hydrotectonic processes

that lead to mineral deposits. Previous studies of these different types of quartz-vein systems have shown that the HASB acted as an overpressured fluid reservoir at mid-crustal levels throughout the Variscan orogenic cycle, in particular during the periods of tectonic inversion in the earliest and late stages of orogeny (Darimont, 1986, Darimont et al., 1988, Kenis et al., 2002, 2005; Van Baelen, 2010; Van Noten et al., 2008, 2011, 2012) (Fig. 1).

To date, four types of quartz-vein systems can be distinguished in the HASB (Fig. 1). Late burial bedding-normal veins (**BNV**)
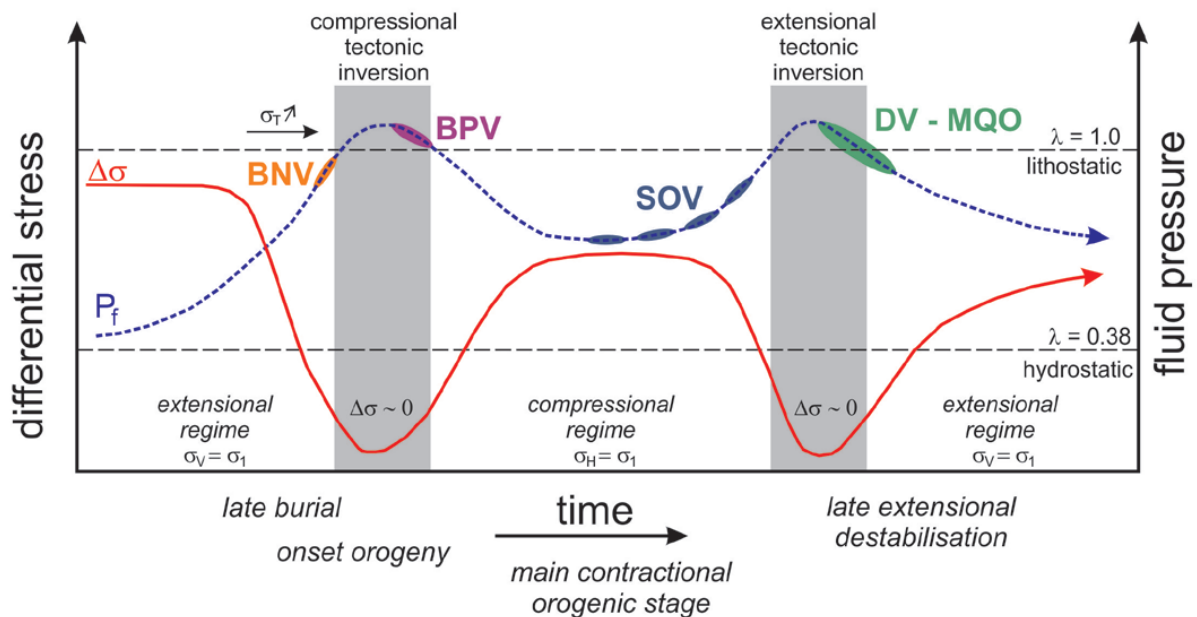
Figure 1: Tentative reconstruction of the stress-state evolution (differential stress vs. fluid pressure) in the HASB during the Variscan orogenic cycle, from late burial in the Ardenne-Eifel rift basin to the late-orogenic collapse of the HASB (after Jacques et al., 2014a; Van Baelen, 2010; Van Noten et al., 2012). The periods of tectonic inversion at the onset of Variscan orogeny (compressional) and in the latest stages of Variscan orogeny (extensional) are indicated. The four types of quartz-vein system, distinguished in the HASB, are marked on this time line. BNV: bedding-normal veins, BPV: bedding-parallel veins; SOV: synorogenic veins; DV: discordant veins; MQO: massive quartz occurrence. σ_1: maximum effective principal stress; σ_V: vertical stress; σ_H: horizontal stress; λ: fluid pressure coefficient (i.e. ratio of fluid pressure to lithostatic pressure); $\Delta\sigma$: differential stress; P_f: fluid pressure.

(Kenis et al., 2002; Van Noten et al., 2011) and early orogenic, bedding-parallel veins (**BPV**) (Van Noten et al., 2008, 2011) materialize the transition of burial in the Ardenne-Eifel rift basin to incipient contraction due to the northwards prograding Variscan deformation front (cf. Fielitz & Mansy, 1999; Sintubin et al., 2009). Both vein systems developed by hydraulic fracturing and are consistently related to low differential stresses and (very) high fluid pressures, up to lithostatic, typical for periods of tectonic inversion (Van Noten et al., 2011, 2012). Synorogenic quartz veins (**SOV**), clearly related to folding and cleavage development, occur rather locally in small-displacement, fold- and fault-related accommodation structures (Jacques et al., 2014a, 2014b). Finally, complex, brittle-plastic discordant veins (**DV**), crosscutting the Variscan cleavage, developed during the late-orogenic destabilization of the slate belt (Van Baelen, 2010). The latter vein system can again be attributed to low differential stresses and high fluid pressures, characterizing the late-orogenic tectonic inversion during the waning stages of orogeny (Van Baelen, 2010).

West of the small village of Mousny, located some 10 km south of La Roche-en-Ardenne, Belgium, a peculiar massive quartz occurrence can be found at the locality called *"Les Blancs Cailloux"* (N50°6'19.23" – E5°36'3.68"). This locality has been known since ancient times, as some archaeological discoveries reveal. It has long been regarded as a site of menhirs or stone circles, known as *cromlechs*, similar to the ones found in France and the U.K. (de Ruette, 1972). Even a legend is associated with the site, telling the story of a malignant shepherd and his herd turned into stone, because the cold-hearted shepherd repeatedly refused water and food to a pilgrim, actually being Jesus of Nazareth in disguise, on his way to the hermitage of Saint-Thibaut (near Marcourt, Belgium).

The reality is, however, less romantic. The **Mousny massive quartz occurrence** (MMQO), exposed at *"Les Blancs Cailloux"*, consists of multiple, >m³-size, milky quartz bodies (Fig. 2). In the fields surrounding the main site, the occurrence of large quartz boulders has also been described (Servaye, 1955, unpublished mapping data, KU Leuven; de Ruette, 1972). Dejonghe & Hance (2001) describe a 250 m broad, NE-SW trending, band of large, up to m³-size, quartz boulders between the main site and the valley of the ruisseau de Cens, located less than 1 km to the SW of the main site. Dejonghe & Hance (2001) and Dejonghe (2008, 2013) interpret this alignment of quartz boulders as indicative of a high-angle, ENE-WSW trending fault, called the Mousny fault (Fig. 3C).

To date, the MMQO has not been thoroughly studied to explain its true nature and possible causes of its strikingly limited spatial occurrence. This study presents the results of a detailed geometrical and kinematic analysis of the massive quartz occurrence, a microstructural analysis of the vein quartz (using both optical and hot cathodoluminescence microscopy), and a geochemical analysis of the fluid inclusions (using both microthermometry and Raman microspectroscopy) to characterize the fluids responsible for the massive quartz occurrence. Such an integrated methodology, giving the opportunity to combine a microstructural analysis with geochemical investigations, has been used frequently to gain insight into the role and evolution of P-T-X conditions during different stages of vein formation and infill (e.g. Becker et al., 2010; Boiron et al., 1996; Boullier & Robert, 1992; Cathelineau et al., 1993; Essarraj et al., 2001; Evans et al., 2012; Jacques et al., 2014a; Lacroix et al., 2011). Eventually, this study will allow to place the MMQO – and similar massive quartz occurrences in the Ardenne-Eifel region – in the overall geodynamic evolution of the HASB.

2. Geological setting

The MMQO is located in the central, epizonal part (Fielitz & Mansy, 1999) of the HASB, SSW of the Lower Palaeozoic Stavelot-Venn basement inlier, forming the backbone of the Ardenne culmination (Fig. 3A). The HASB consists of Lower Devonian, siliciclastic, predominantly argillaceous metasediments, affected by a low-grade metamorphism, considered to have a burial origin and to be pre- to synkinematic with respect to the prograding Variscan deformation (Fielitz & Mansy, 1999). The main structural feature in the HASB is a pervasive slaty cleavage with regionally a rather consistent attitude. The thick Lower Devonian sequence of the slate belt reflects rapid syn-rift sedimentation particularly active during the Pragian (ca. 410 Ma; Oncken et al., 1999). The HASB is part of the Ardenne allochthon, a major allochthonous domain, which thrusted over its foreland, the Brabant parautochthon, during the latest – Asturian – stage (late Carboniferous; ca. 300 Ma) of the Variscan orogeny (Mansy & Lacquement, 2002; Meilliez & Mansy, 1990). Deformation in the HASB, however, occurred during the earlier – Sudetic – stage (middle Carboniferous; ca. 325-310 Ma) of the Variscan orogeny (Fielitz & Mansy, 1999). The Ardenne allochthon represents the northern frontal parts of the Rhenohercynian foreland fold-and-thrust belt, at the northern extremity of the Central European Variscides (Oncken et al., 1999).
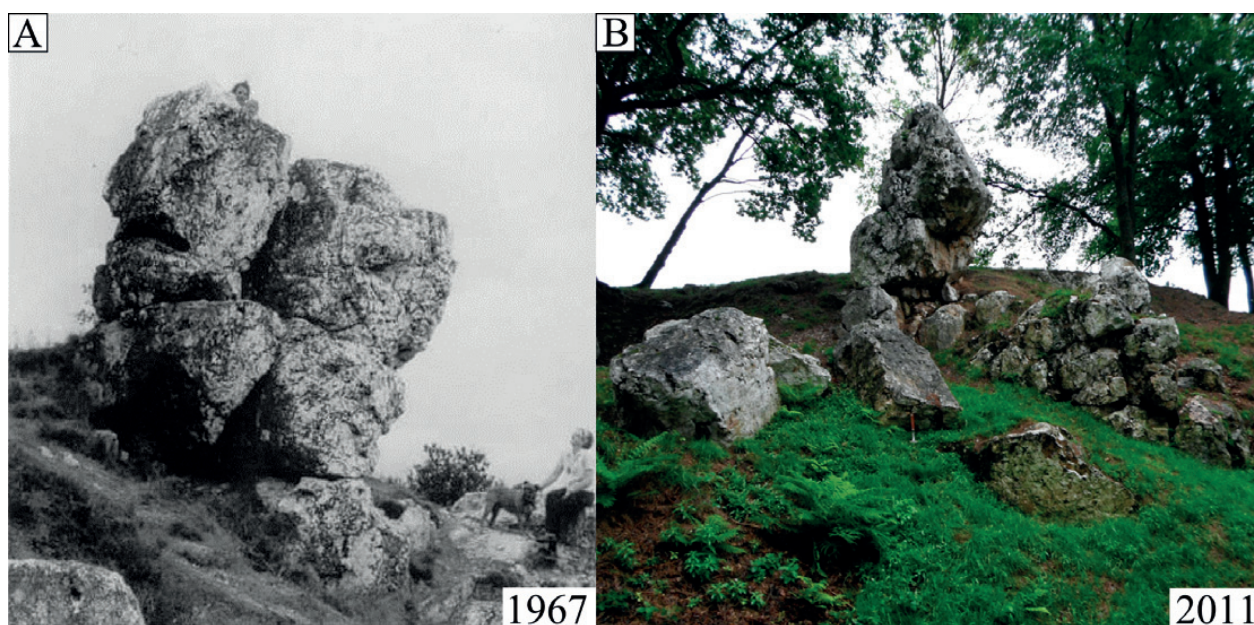
Figure 2: *"Les Blancs Cailloux"*, main site of the Mousny massive quartz occurrence (MMQO). The site has been subject to artisanal mining, eventually leading to a decline of the exposure over the years, as exemplified by the two photographs 44 years apart (Photograph 1967 courtesy of Annet-Vandries, Ortho, Belgium; Photograph 2011 courtesy of Depoorter).
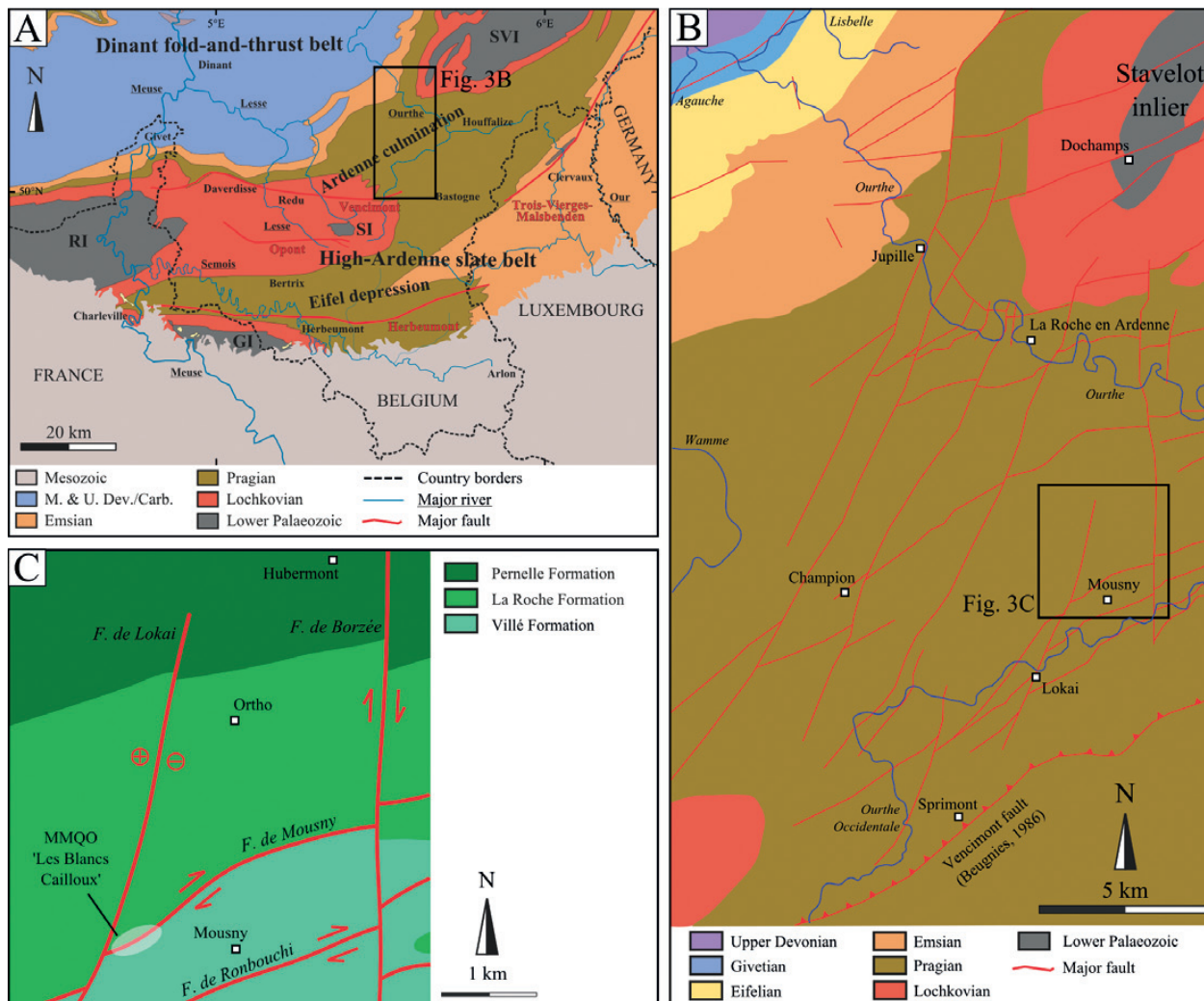
Figure 3: (A) Geological map of the southeastern part of the Ardenne-Eifel area displaying the main tectonostratigraphical units (after Asselberghs, 1946). RI, SVI, SI, GI: Rocroi, Stavelot-Venn, Serpont and Givonne basement inliers, respectively. (B) Geological map of the central part of the Ardenne culmination SSW of the Stavelot-Venn basement inlier, coinciding with the SSW extremity of the so-called "Ourthe zone", with indication of major inferred fault traces (red) and rivers (blue) (adapted after Dejonghe, 2008). See Fig. 3A for the location. (C) Detailed geological map of the Mousny area (after Dejonghe, 2008) with indication of *"Les Blancs Cailloux"*, the main site of the MMQO. See Fig. 3B for the location.

Mousny is furthermore located at the SSW extremity of the so-called "Ourthe Zone" (Hance et al., 1999; Meilliez et al., 1991) or "Ourthe Virgation Zone" (Szaniawski et al., 2003), a ca. 10 km wide, NNE-SSW trending zone bordering the Lower Palaeozoic Stavelot-Venn basement inlier to the west (Fig. 3B). This zone is interpreted as the expression of a buried buttressing lateral ramp causing transpressional deformation within the overriding allochthonous domain. Towards its SSW extremity this transpressional deformation seems materialized by a series of inferred NNE-SSW trending, dextral, strike-slip faults (Dejonghe, 2008) (Fig. 3B). According to Dejonghe (2008) these faults are considered to displace a series of inferred ENE-WSW trending, normal faults with a dextral, strike-slip component (Fig. 3B). The latter faults are typified by quartz deposits. The MMQO has therefore been interpreted by Dejonghe (2008) as exemplary for the quartz deposits linked to one of the latter type of faults, the so-called Mousny fault (Dejonghe & Hance, 2001) (Fig. 3C).

In the wider Mousny area, rocks of the Lower Devonian Villé, La Roche and Pèrnelle Formations (Bultynck & Dejonghe, 2001; Dejonghe & Hance, 2001) are exposed (Fig. 3C). These formations are Pragian to early Emsian in age. The Villé Formation consists of dark shales intercalated with rusty brown laminated sandstone layers, blue sandstones and fossiliferous bluish carbonate-rich sandstones. The La Roche Formation is predominantly composed of blue shales interlayered with light blue sandstones and quartzitic sandstones, red sandstones and blue green fossiliferous siltstones. The Pèrnelle Formation is made up of massive, green blue sandstones and metasandstones

interlayered with thin dark shales and siltstones (Bultynck & Dejonghe, 2001; Dejonghe & Hance, 2001).

3. Structural analysis

The study area surrounding the MMQO is very poorly exposed. Only some road cuts and outcrops in the valleys provide crucial information to constrain the kinematic context of the massive quartz occurrence. The structural analysis primarily consists of a detailed mapping of all relevant structural features at the main site of *"Les Blancs Cailloux"*. 11 vein-quartz samples (*AR11SD001-011*) were taken for further analysis (Figs 4 & 5).

Based on the mapping exercise of Servaye (1955; unpublished data KU Leuven) a number of outcrops, exposing quartz veins, in the nearest proximity of the main site, were selected to better constrain the overall kinematics of all quartz occurrences in this part of the HASB. 13 vein-quartz samples (*AR11SD012-024*) were taken in the wider Mousny area for this purpose (Fig. 4).

Orientation measurements were taken with a Freiberg compass and are given in dip direction–dip for planar features (e.g. bedding, cleavage, fault, joint) and trend–plunge for linear features (e.g. lineation, fold hinge line, slip line). The orientation analysis has been performed using OpenStereo software of Grohmann & Campanha (2010). Microphotographs were taken using a Leica DMLP microscope connected to a DeltaPix DP200 digital camera.
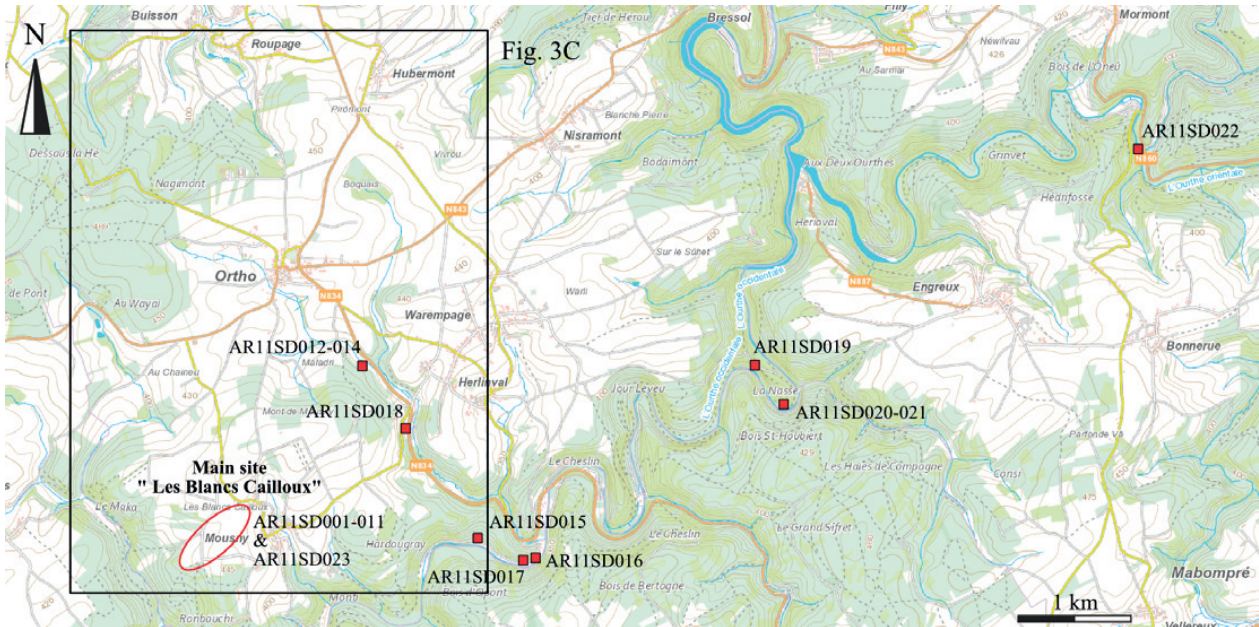
Figure 4: Topographic map indicating the sampling sites of all studied veins, relative to the location of the main site of the MMQO at *"Les Blancs Cailloux"*. Fig. 3C is indicated as reference.
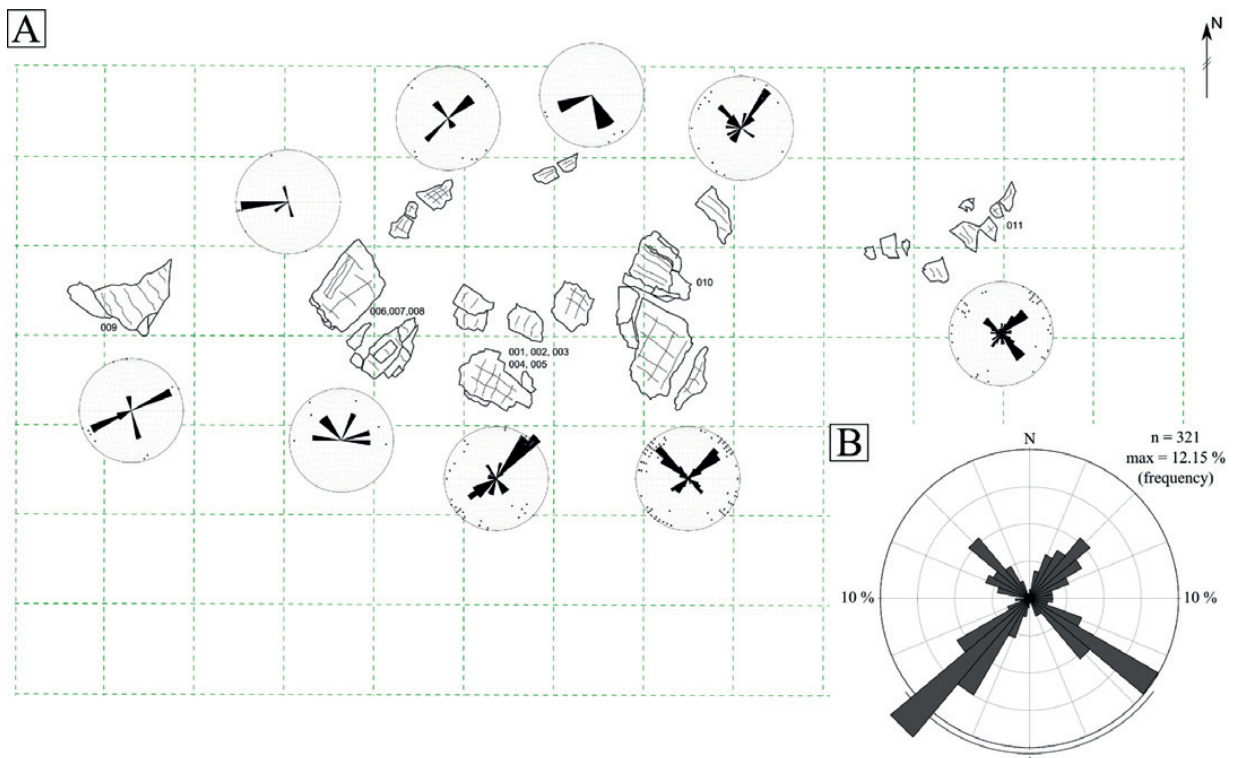

Figure 5: Main site – *"Les Blancs Cailloux"* (A) Detailed map of the individual quartz bodies of the MMQO, each time with the rose diagram of the joint orientations. Sample locations are indicated with numbers 001 to 011. Grid width is approximately 5 m. (B) Rose diagram of all joint sets measured (n = 321).
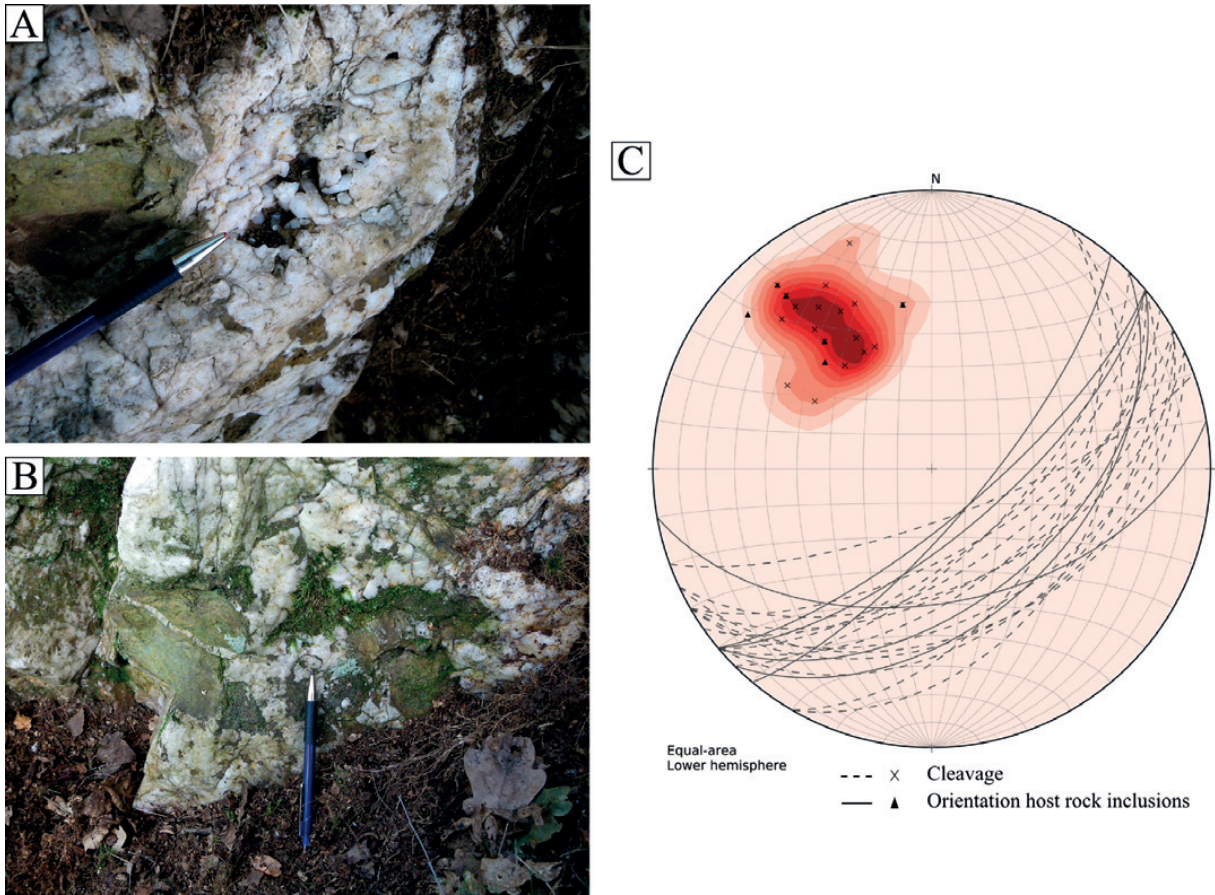
3.1. Main site – "Les Blancs Cailloux"

The main site consists of some 30, >m³-sized, bodies of massive milky quartz, spread over an area of approximately 2300 m² (Fig. 5). Most surfaces of the quartz bodies show a slight rusty brown discoloration due to the presence of iron-oxides. Inside the milky quartz matrix, geodes of clear quartz are recognized (Fig. 6A).

Within the individual quartz bodies, host-rock fragments can be identified (Fig. 6A-B). These host-rock fragments are rusty brown, sandstone and grey-greenish siltstone fragments. Most probably they can be attributed to the Villé Formation as described by Bultynck & Dejonghe (2001). Some host-rock fragments

contain quartz veins (Fig. 6B). All host-rock fragments are rather elongated, approximately parallel to the internal cleavage. They, moreover, show a very consistent attitude, which is very similar to the average regional cleavage attitude (145/55) as measured in neighbouring outcrops (Fig. 6C).

Two, roughly orthogonal, sets of sub-vertical joints (dip 85-90°) can be identified on the different quartz bodies: one set with an overall N40W strike and another set with an overall N40E strike (Fig. 5B). One or both of these joint sets are consistently present on each of the individual bodies (Fig. 5A), supporting the basic assumption that all studied quartz bodies are effectively in situ. This is also corroborated by the consistent attitude of the host-rock fragments (Fig. 6C).

Figure 6: Main site – *"Les Blancs Cailloux"* (A-B) Examples of host-rock fragments, with thin quartz veinlets (**Q1a**), inside the milky quartz matrix of the MMQO (**Q1b**). A geode (**Q1c**) is marked in (A) with a pencil. The pencil is ca. 15 cm long. (C) Lower-hemisphere equal-area projection of cleavage and host-rock fragment orientation measurements. Dotted lines: great circles of cleavage planes (n = 12); full lines: great circles of host-rock fragment orientation (n = 6). Contours indicate the best-fit solution for the regional cleavage attitude.

3.2. Other outcrops

Two types of quartz vein were observed in the outcrops in the wider area surrounding the MMQO (Fig. 4). A first type of quartz vein, which is the predominant one, is oriented sub-parallel to the regional cleavage or is slightly crosscutting it (at an angle of no more than 10°) (Fig. 7A-B). These cleavage-parallel veins also show some pinch-and-swell characteristics, indicating some degree of vein-parallel stretching. The specific temporal relationship with respect to the cleavage allows to identify these cleavage-parallel veins as syn- to late-orogenic veins (Fig. 1).

A second quartz-vein type consists of a set of bedding-normal, interboudin veins in a competent metasandstone layer (ca. 5 cm thick), embedded in incompetent metapelites (Fig. 7C). Vein spacing is ca. 10 cm. The aspect ratio of ½ of the sandstone segments in between the veins typically results from the process of boudinage, i.e. layer-parallel stretching of the metasandstone layer (Van Noten & Sintubin, 2010). In the HASB, such interboudin veins typically occupy small-displacement, fold- and fault-related accommodation structures that develop during the
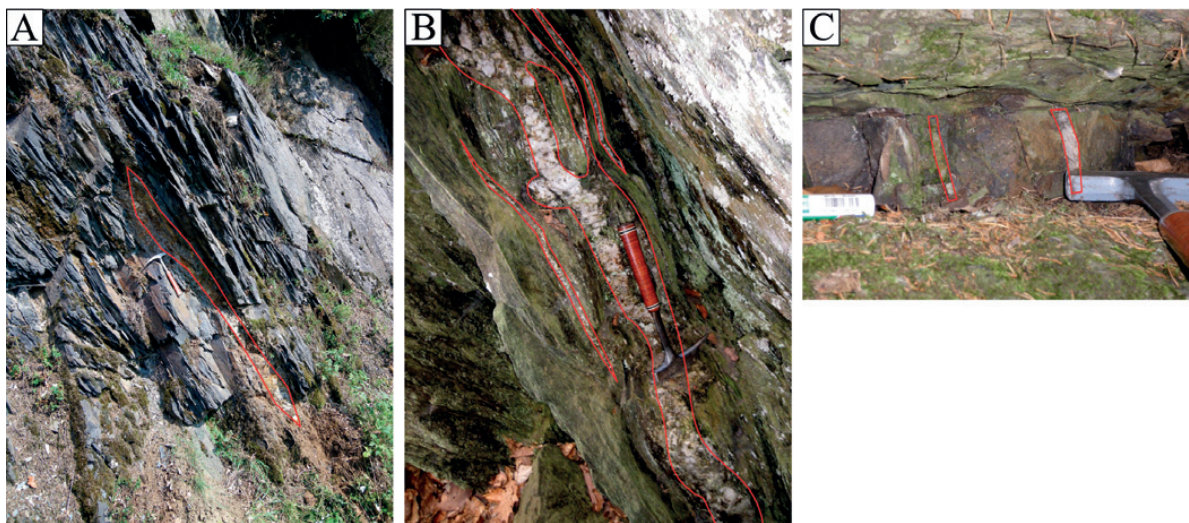
Figure 7: (A) Cleavage-parallel vein (traced with full red lines) (**Q2**), with an attitude of 150/55 (samples *AR11SD012 & 013*). (B) Vein (180/50) cross-cutting the cleavage (170/50) at a very small angle (samples *AR11SD020 & 021*) (**Q2**). (C) Bedding-normal, interboudin veins (sample *AR11SD016*) (**Q0**). Hammer for scale (33cm). See Fig. 4 for location.

main contractional stage of orogeny (Jacques et al., 2014b; Van Baelen & Sintubin, 2008). Therefore, these veins are considered synorogenic in nature (**SOV**; Fig. 1).

4. Petrography

Based on the field evidence, already a number of quartz-vein types can be identified and classified chronologically, i.e. (1) the interboudin veins (**Q0**), (2) the massive quartz occurrence (MMQO) (**Q1**), and (3) the cleavage-parallel veins (**Q2**). The particular attitude of the host-rock fragments, i.e. parallel to the regional cleavage attitude, suggests already a possible genetic relationship between the cleavage-parallel quartz veins (**Q2**) and the massive quartz occurrence (**Q1**).

4.1. Microscopy

4.1.1. The MMQO (Q1)

The milky quartz matrix of the MMQO primarily consists of large, sub- to anhedral quartz crystals with moderately irregular grain boundaries. Crystal size varies from small and granular (mm-scale and smaller) to large and elongate (cm and upwards) (Fig. 8A).

Most of the quartz displays undulose extinction (Fig. 9A) with some transition towards subgrain boundaries as well as elongate subgrains (Fig. 9B). Most quartz crystals have irregular, serrated grain boundaries (Fig. 9B-C). In some samples, the boundaries between crystals are lined with small, granular quartz crystals displaying the same interference pattern as the neighbouring crystals (Fig. 9C). Sometimes, this lining is so well-developed that it gives rise to core-and-mantle microstructures. These microstructures are indicative of bulging recrystallization and, to a lesser extent, grain boundary migration recrystallization (Passchier & Trouw, 2005). Other samples show a highly fractured, mosaic breccia microfabric (Fig. 8B). Brecciation seemingly occurred after crystal-plastic deformation of large quartz crystals, already affected by undulose extinction or subgrain boundary development.

In the host-rock fragments, several crosscutting relationships can be observed between different quartz generations (Fig. 8C). Thin veinlets in the host-rock fragment contain mostly elongate-blocky crystals as opposed to the sub- to anhedral, blocky quartz crystals in the milky quartz matrix (Fig. 8C).

Eventually, three, chronologically distinct, quartz-growth generations can be identified in the MMQO (**Q1**): the thin veinlets (**Q1a**) within the host-rock fragments, crosscut by veins related to the main, milky quartz matrix (**Q1b**) (Fig. 8C), and both geode infill and bands of clear quartz (**Q1c**) within the milky quartz matrix (**Q1b**).
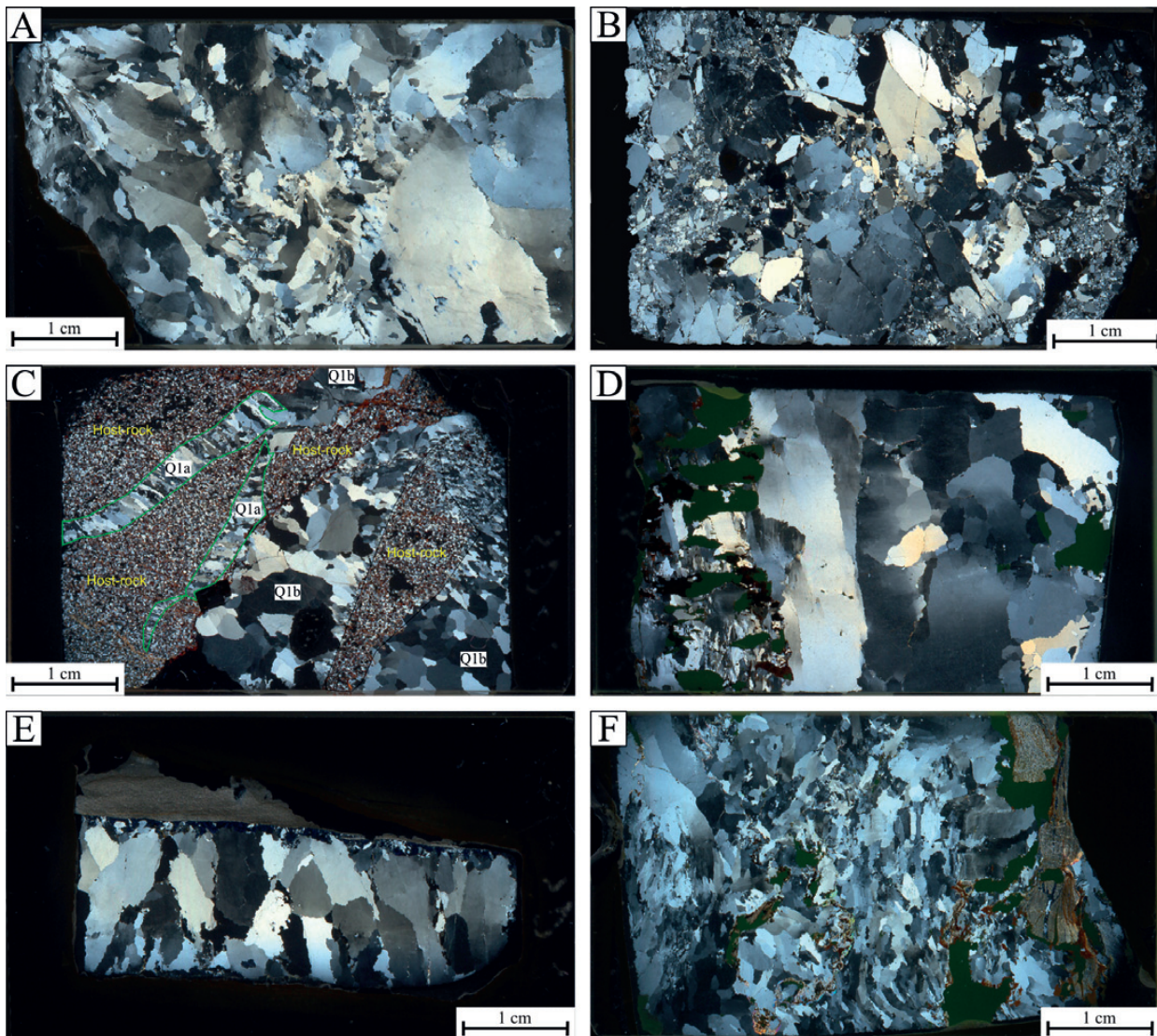
Figure 8: Micrographs of vein quartz in the MMQO (**Q1**) (A-C) and in the cleavage-parallel veins (**Q2**) (D-F). All micrographs with crossed polars. (A) Highly strained quartz crystals showing a sweeping, undulose extinction and several subgrains (*AR11SD008*). (B) Brecciated vein (*AR11SD001*). (C) Microstructural relationship between the **Q1b** and **Q1a** vein generations within the host-rock fragments (*AR11SD007*). (D) Blade-like quartz crystals at the vein wall in the **Q2** quartz generation (*AR11SD014*). (E) Chlorite concentration at the vein wall in the **Q2** quartz vein (*AR11SD020*). (F) Highly-strained **Q2** quartz near the vein wall (host rock to the right of the micrograph) (*AR11SD012*). See Figs **4** and **5** for sample location.

4.1.2. Cleavage-parallel veins (Q2)

The vein quartz in the cleavage-parallel veins show all the characteristics of the milky quartz matrix (**Q1b**) of the MMQO. The veins consist of predominantly large sub- to anhedral quartz crystals with moderately irregular grain boundaries, showing undulose extinction, subgrain boundaries, bulging, and core-and-mantle microstructures (Fig. 8D), all indicative of bulging recrystallization and, to lesser extent, grain boundary migration recrystallization (Passchier & Trouw, 2005). In contrast to the **Q1b** quartz matrix, the crystals appear, however, to be more elongate in the cleavage-parallel veins (Fig. 8E), in particular near the vein wall.

Besides quartz, some samples also contain muscovite and chlorite, causing the formation of pinning microstructures and stylolite-like features (Fig. 8E-F and Fig. 9D-E). Both minerals are believed to have precipitated at different times relative to the quartz precipitation. Chlorite primarily occurs at the contact between the quartz body and the host rock (Fig. 9F), suggesting an early precipitation at the onset of veining. Muscovite occurs throughout the quartz mass in between quartz crystals and thus seems to have precipitated contemporaneously with the milky quartz. Some evidence has been found of a late pore-filling carbonate precipitate. Additionally, dispersed in both the quartz mass and host-rock fragments, opaque minerals, hematite, sphalerite and sometimes chalcopyrite, are present. These accessory minerals, and their microstructural relationships with the quartz crystals, were also observed in the MMQO (**Q1**).

There is further evidence for a second quartz generation (**Q2b**) later than the bulk vein quartz (**Q2a**) within the cleavage-parallel veins. One sample (*AR11SD014*) contains a geode of transparent quartz (**Q2b**) inside the vein matrix (**Q2a**) with the wall of the geode lined with muscovite blades (Fig. 9E). Nearly all collected samples contain host-rock fragments, however, without any internal veinlets.

4.1.3. Interboudin veins (Q0)

The crystal size in the bedding-normal, interboudin veins is generally smaller than in the MMQO and the cleavage-parallel veins. Quartz crystals generally show undulose extinction and, although limited, some degree of grain boundary migration. Only in this vein generation, plagioclase has been observed.

4.2. Hot cathodoluminescence

Several of the collected samples were analyzed by hot cathodoluminescence microscopy. The device used is a Heinzinger PNC 20000-3neg and a Simon Neuser HC3-LM/SG, run at 13.5kV and 0.15 µA, connected to an Olympus Lumic HC3-LM microscope (KU Leuven). To overcome the problem of colour shift during cathodoluminescence measurements, 6 successive photographs were taken, one with transmitted light and 5 recording the luminescence behaviour with 1 minute interval and exposure time of 10 sec. This procedure guarantees a relatively good estimation of the initial luminescence colour, enabling to detect possible differences in luminescence between samples. More information on the procedure can be found in Boggs & Krinsley (2006), Götze (2012) and Pagel et al. (2000).

All samples of the MMQO show an initial dark blue luminescence that rapidly declines and shifts towards a red-

Figure 9: Microstructures observed in the different vein samples. All micrographs with crossed polars. (A) Undulose extinction, slightly sweeping (**Q1**) (*AR11SD003*). (B) Elongate subgrains (**Q1**) (*AR11SD006*). (C) Bulging recrystallization visible at grain boundaries (**Q1**) (*AR11SD001*). (D) Pinning microstructure due to muscovite crystals (**Q2**) (*AR11SD012*). (E) Crystals of clear quartz (**Q2b**) embedded inside the cloudy quartz (**Q2a**), with muscovite blades at the contact (*AR11SD014*). (F) Presence of chlorite at the vein wall (**Q2**) (*AR11SD020*). See Figs 4 and 5 for sample location.
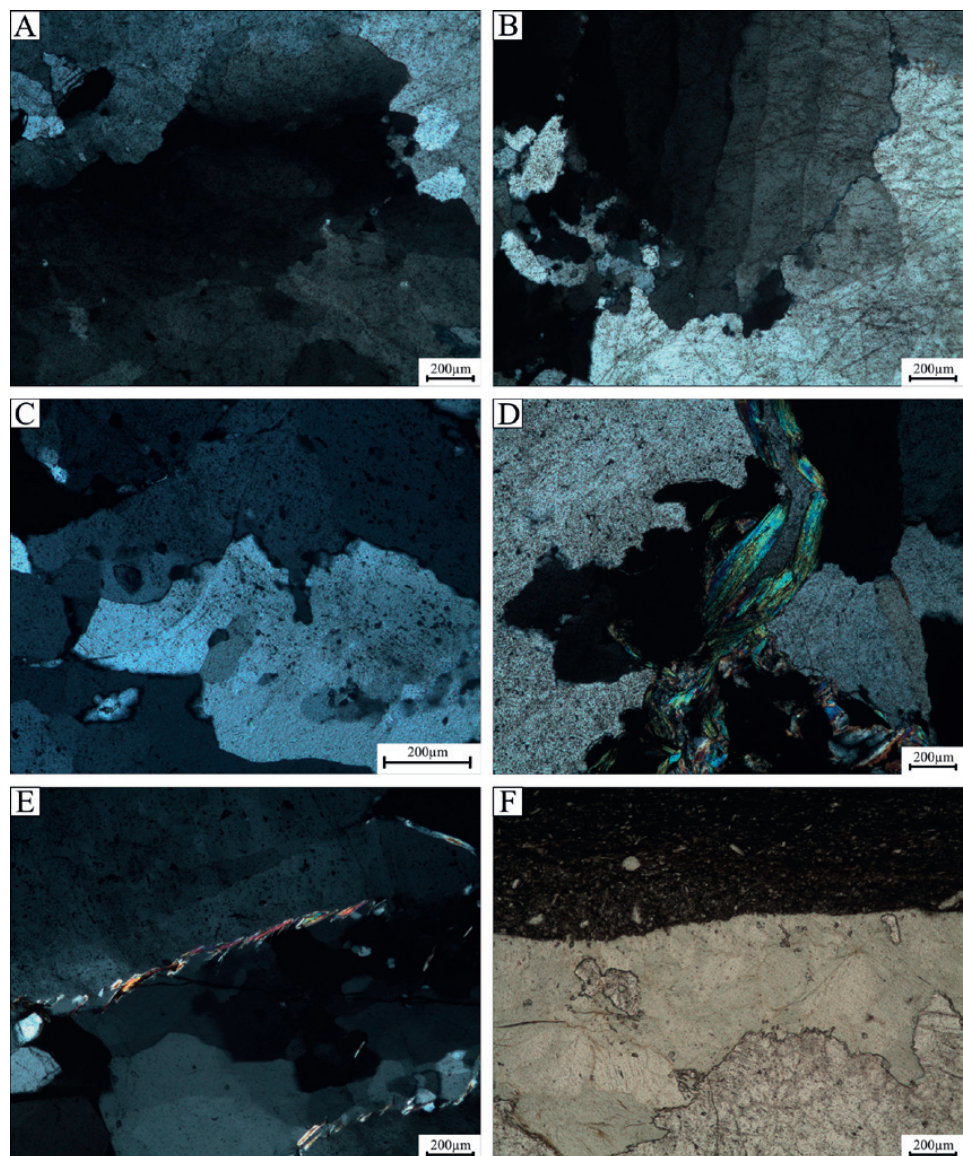
brown luminescence, typical of low-grade metamorphic and hydrothermal quartz (Dietrich & Grant, 1985; Götte & Richter, 2006). In samples of the milky quartz matrix (**Q1b**) typical luminescence features can be observed besides the strong colour shift ant the dominant blue colour (Fig. 10A). Relic crystals with clear indication of growth zones can be identified. These growth zones show light blue luminescence and represent a first sub-stage (**A**) of **Q1b**. These growth zones in turn are truncated by quartz with dark blue luminescence (**B**), and subsequently, both are crosscut by a complex array of fractures (**C-D**), subsequently filled with dark blue luminescent quartz (Fig. 10A). Hence, at least four sub-stages can be identified within the milky quartz matrix **Q1b**. The more transparent quartz (**Q1c**), filling geodes inside the dusty quartz matrix (**Q1b**) (sample *AR11SD005*), does not really show a clear difference in cathodoluminescence with the surrounding quartz mass. The quartz filling of a micro-geode in the cleavage-parallel vein quartz (**Q2b**) (sample *AR11SD014*) shows, however, a clear yellowish-green luminescence in contrast to the dark to bright blue cathodoluminescence of the quartz matrix (**Q2a**) (Fig. 10B). This cathodoluminescence difference may be due to a changing fluid composition during filling of the cavities.

5. Geochemical analysis

5.1. Fluid inclusion microthermometry

A microthermometric analysis has been performed on five samples, of which a ca. 150 μm thick wafer has been prepared. Three samples were taken from the MMQO (**Q1**) (*AR11SD001, AR11SD005 & AR11SD010*), one sample from a cleavage-parallel vein (**Q2**) (*AR11SD012*) and another one from an interboudin vein (**Q0**) (*AR11SD016*) (see Figs 4 and 5 for sample location). Fluid inclusions were analyzed using a standard Olympus microscope fitted with either a MDSG 600 or a THMSG 600 Linkam heating/cooling stage (KU Leuven). The stage was calibrated with Syn Flinc™ synthetic fluid inclusions at -56.6 °C, -21.2 °C, -10.6 °C, 0.0 °C and at 374.1 °C. Reproducibility of the measurements was around 0.2 °C for the melting temperatures and around 3 °C for homogenization temperatures.

Two-phase inclusions of variable sizes were predominantly observed in all samples. When present, primary fluid inclusions within growth zones (when not deformed, stretched or leaked), were selected. In other cases, care has been taken to select isolated fluid inclusions or fluid inclusion assemblages (FIAs) that are not distributed within a three-dimensional plane (i.e. secondary microcracks) and randomly come into focus, so that a primary or pseudosecondary origin is likely.

5.1.1. MMQO (Q1)

Within samples *AR11SD001* and *AR11SD005*, different occurrences of fluid inclusions are observed in the milky quartz

crystals (**Q1b**): clusters, isolated inclusions, and trails related to microcracks. Nearly all are two-phase inclusions. The size of the inclusions (< 2 μm to 10 μm), as well as their vapour-liquid ratio (5 to 80% vapour) is strongly variable, even within a single FIA. The shape of the inclusions is also very variable with some displaying highly angular morphologies. Both this irregular shape and the very variable vapour-liquid ratio indicate that the fluid inclusions were deformed and leaked during and/or after quartz precipitation. Within the **Q1b** quartz of sample *AR11SD010* also two-phase inclusions with a variable size (< 5 μm to 30 μm) were observed. These inclusions, however, display a constant phase ratio (20-30% gaseous bubble and 70-80% aqueous liquid). Some fluid inclusions can be identified occurring in planes within primary growth zones. In between these, some isolated inclusions, showing a random and clustered occurrence, can also be considered as primary or pseudosecondary.

For the primary/pseudosecondary inclusions within the **Q1b** quartz of these three samples, two main types of inclusions can be discriminated based mainly on cooling-heating behaviour. A first type of microthermometric behaviour accounts for mixed aqueous-gaseous inclusions (**F1**). This type of inclusions is observed in all three samples. Upon cooling from room temperature, however, different phase transitions are observed in samples *AR11SD005* and *AR11SD010*. The *AR11SD005* inclusions display the nucleation of a small vapour bubble inside the larger gaseous liquid phase upon cooling. Upon further cooling, three additional phase transitions are observed. First, clathrates are formed in the rim around the large gaseous liquid phase, followed by the freezing of the aqueous liquid, and finally freezing of the gaseous liquid (ca. -100 °C). These transitions indicate the presence of CO_2 and possibly other gases inside the inclusion (Murphy & Roberts, 1997). Upon heating, again several phase transitions are identified. First, the melting of CO_2 ($TmCO_2$) is observed between -63.6 and -59.5 °C (Fig. 11A). This departure from the melting temperature of pure CO_2 (-56.6 °C) indicates the presence of other gases besides CO_2 (Van den Kerkhof & Thiéry, 2001). Further heating displays the final melting of ice (TmIce) and final melting of the clathrate (TmClath), with TmIce ranging between -10.3 and 5.9 °C (Fig. 11B) and TmClath ranging between 5.2 and 12.5 °C (Fig. 11C). The range in TmIce values with positive numbers indicate metastable melting and are unreliable. The homogenization temperature of CO_2 ($ThCO_2$) was also determined (the disappearance of the second bubble after nucleation) and lies between -13.7 and 4.7 °C (Fig. 11D). Total homogenization temperatures (Thtot) for these aqueous-gaseous inclusions were difficult to determine as decrepitation occurred from 240 °C. The three measured inclusions give a Thtot of 336, 346 and 354 °C, respectively (Fig. 11E).

The mixed aqueous-gaseous inclusions of sample *AR11SD010* (**F1**) display a more limited amount of phase transitions upon cooling. A third phase does not appear upon cooling, limiting the
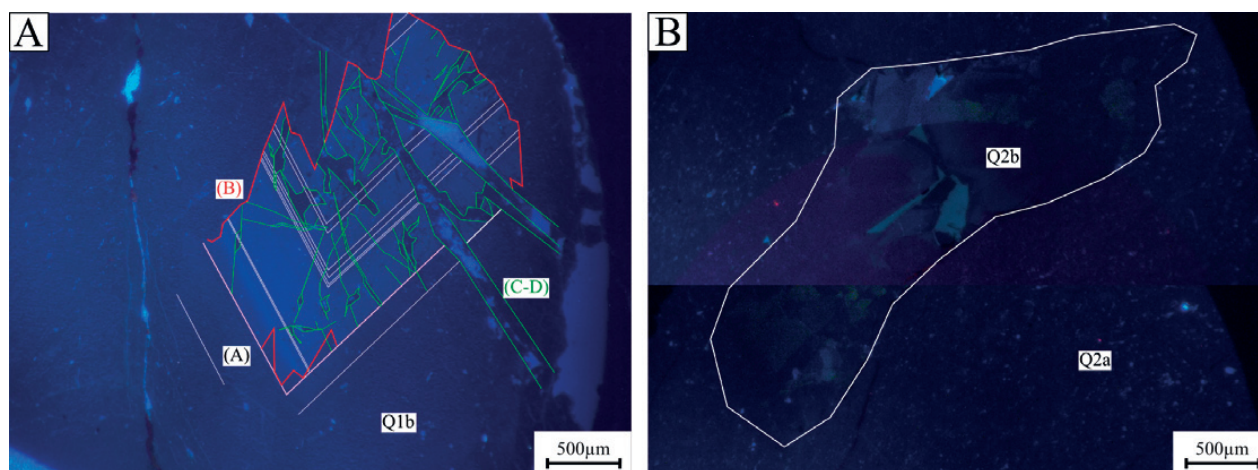
Figure 10: Micrographs taken with hot cathodoluminescence. (A) **Q1b** stages: Relict of a grain displaying growth zones (A - white) with signs of overgrowth (B - red) and fracturing and infill (C&D - green) (*AR11SD001*). (B) Microgeode (**Q2b**) within a matrix of milky quartz (**Q2a**) (*AR11SD014*). See Figs 4 and 5 for sample location.

observed phase transitions to clathrate formation and freezing of the aqueous liquid. First melting (Tfm) is difficult to detect, and only a limited number of measurements was collected around -21 °C, indicating the presence of NaCl in the aqueous liquid. TmIce occurs between -4.3 and -3.0 °C (Fig. 11B) and TmClath between 5.1 and 9.1 °C (Fig. 11C). These values indicate a maximum salinity that ranges between 4.5 and 6 eq. NaCl wt% (Fig. 11G). Thtot ranges between 229 and 291 °C (Fig. 11E). Decrepitation occurred from 200 °C onwards.

Because of the decrepitation and leakage (e.g. the very variable vapour-liquid ratio and large range in ThCO$_2$ - Fig. 11D) of the *AR11SD005* inclusions, having influenced the composition of these aqueous-gaseous inclusions, they will not be used further in the discussion on P-T conditions during veining. The homogenization temperatures for these inclusions, to which a pressure correction has not yet been applied, are too high considering the maximum metamorphic temperature of the study area (i.e. 350 °C – see paragraph 7.3). Hence, the here presented microthermometric results provide a general idea on the inclusion type present and its behaviour upon cooling-heating. Instead, the more reliable microthermometric results of *AR11SD010* will be used in further discussions on P-T conditions.

A second inclusion type consists of aqueous fluid inclusions (**F2**), which are retrieved in all three samples *AR11SD001, AR11SD005* and *AR11SD010*. Upon cooling of these inclusions,

a partial or complete collapse of the vapour bubble was observed. First melting temperatures, although difficult to observe, were evidenced at ca. -21 °C, indicating a H$_2$O-NaCl composition. Final melting temperatures lie between -4.0 and -0.2 °C (Fig. 11F), corresponding to salinities between 0.4 and 6.4 eq. NaCl wt% (Fig. 11G) (Potter et al., 1978). Homogenization temperatures range from 111 to 184 °C (Fig. 11E).

More transparent quartz, belonging to the early stages of the **Q1c** quartz, is less crowded with fluid inclusions, which also appear to be less deformed. The phase ratio is, however, variable. The samples contain many angular and irregular inclusions. The size varies from <5 μm to 30 *μ*m, with a volume range from 5 to 70% for the gas-bearing bubble. Upon cooling of these inclusions, again a partial or complete collapse of the vapour bubble was observed. First melting temperatures around -21 °C suggest a H$_2$O-NaCl composition. Final melting temperatures of ice lie between -6.6 and -0.3 °C (Fig. 11F), corresponding to a salinity between 0.5 and 9.9 eq. NaCl wt% (Fig. 11G). Thtot for these aqueous inclusions lies between 112 and 191 °C (Fig. 11E). The similar composition and homogenization temperatures of these inclusions and the aqueous inclusions measured in the more deformed **Q1b** matrix quartz, indicate that both belong to the **F2** fluid type. While in the cloudy **Q1b** quartz both aqueous (**F2**) and aqueous-gaseous (**F1**) inclusions were retrieved, the clear **Q1c** quartz only contains aqueous inclusions (**F2**).

Figure 11: Results from microthermometric analysis. (A) CO$_2$ melting temperatures (TmCO$_2$). (B) ice melting temperatures (TmIce) for aqueous-gaseous inclusions. (C) Clathrate melting temperatures (TmClath). (D) CO$_2$ homogenization temperatures (ThCO$_2$). (E) Total homogenization temperatures (Thtot). (F) Ice melting temperatures (TmIce) for aqueous inclusions. (G) Salinity of the **F1** type fluid, specified for sample *AR11SD005* (in red) and sample *AR11SD010* (in green), and the **F2** type fluid in general (in grey).
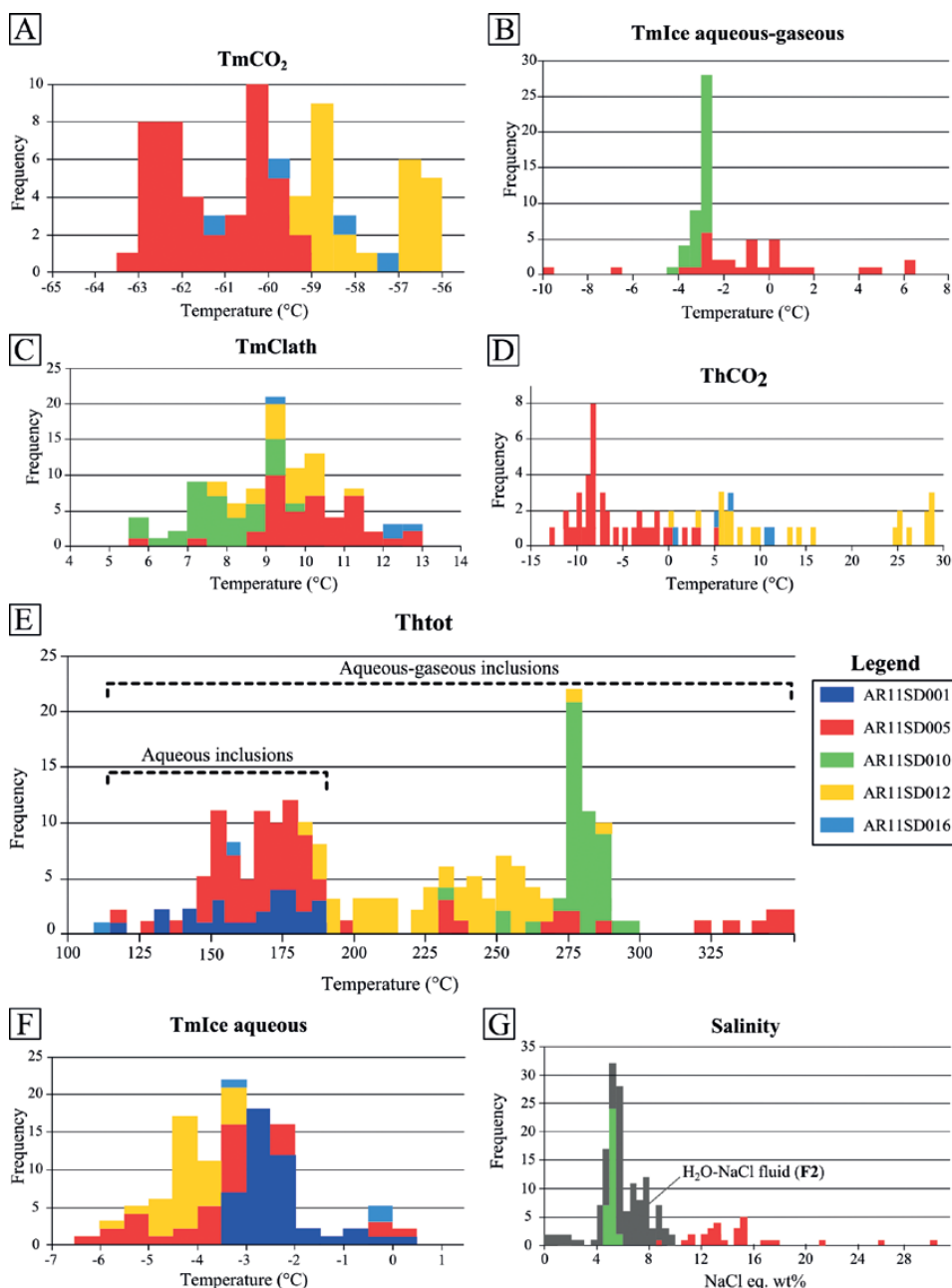
5.1.2. Cleavage-parallel veins (Q2)

Similar to the quartz of the MMQO the amount of fluid inclusions in the cleavage-parallel veins (sample *AR11SD012*) is very high, although the latter appear to have a less cloudy quartz matrix. The inclusions are predominantly two-phase, sometimes three-phase, have very variable liquid-vapour ratios and are generally smaller (from <5 μm to 10 μm) than the ones observed in the MMQO samples. It is not possible to distinguish primary from pseudosecondary and secondary inclusions. Again two types of fluid inclusions, mixed aqueous-gaseous and aqueous inclusions, are retrieved.

The mixed aqueous-gaseous inclusions (**F1**) display multiple phase transitions on cooling, as well as $TmCO_2$ and TmClath on heating from -120 °C. Some of these inclusions display three phases at room temperature, others show a bubble nucleating on cooling inside the gaseous liquid phase. $ThCO_2$ and TmClath overlap for these inclusions, with $ThCO_2$ ranging from 2.7 to 28.5 °C (Fig. 11D), and TmClath ranging from 1.5 to 10.6 °C (Fig. 11C). The measured range for Thtot lies between 180 and 281 °C (Fig. 11E). The large range in vapour-liquid ratio, Thtot and $ThCO_2$, in combination with the very variable behaviour upon cooling and heating, indicate that the aqueous-gaseous inclusions of *AR11SD012* are strongly deformed and leaked. As such, the microthermometric results for this inclusion type will not be used in further discussion on P-T conditions of veining.

The aqueous inclusions (**F2**) display a partial collapse of the bubble on freezing and show a first and final melting of ice. A first melt was observed around -21 °C, indicating a H_2O-NaCl composition, and final melting lies between -6.1 and -3.5 °C (Fig. 11F), corresponding with salinities between 5.8 and 9.4 eq. NaCl wt% (Fig. 11G).

5.1.3. Bedding-normal veins (Q0)

The quartz crystals contain much smaller fluid inclusions (5 μm and lower) than any of the other samples. Most of them appear to be two-phase, but due to the small size this distinction is difficult. The small size is also the reason why only a few measurements could be made on this sample (*AR11SD016*).

On cooling down from room temperature, the inclusions display a nucleation of a third phase and a solidification of the CO_2 phase around -100 °C. These two phase transitions again point to the presence of gaseous components inside these inclusions. Upon heating from -120 °C, CO_2 and clathrate melting was observed. The range for $ThCO_2$ is between 0.3 and 11.0 °C (Fig. 11D), for $TmCO_2$ between -61.6 and -57.7 °C (Fig. 11A) and for TmClath between 9.0 and 12.1 °C (Fig. 11C). Only few Thtot were measured as decrepitation occurred readily. The two inclusions that were measured yielded a Thtot of 112 and of 155 °C (Fig. 11E). The depression of the melting point compared to pure CO_2 (-56.6 °C) again indicates the presence of other gases.

5.1.4. Summary

Compiling the different microthermometric measurements, some conclusions can be made on the different fluid types. Two main types of fluids have been defined: an aqueous-gaseous fluid (**F1**), and an aqueous fluid with a H_2O-NaCl composition (**F2**). The Thtot shows a wide range (Fig. 11E). While the aqueous fluid inclusions (**F2**) are relatively limited to a distribution range of ca. 125-190 °C, the aqueous-gaseous inclusions show a very large range of ca. 115-350 °C (Fig. 11E). This wide range of Thtot is most likely related to the measurement of leaked inclusions, which also affects the composition and density of the mixed aqueous-gaseous inclusions. Hence, the smaller temperature range for the aqueous fluid inclusions is explained by the lesser amount of deformation observed for the assemblages in question (i.e. the clear quartz of **Q1c**). A relatively well-defined temperature range is retrieved for the *AR11SD010* aqueous-gaseous inclusions, which show a narrow homogenization temperature distribution of 270-300 °C (Fig. 11E). These inclusions are therefore considered to represent the original formation temperatures and will, together with the aqueous inclusions, be used to retrieve the P-T conditions of trapping for both the **F1** and **F2** fluid phases. The other measurements are discarded.

As mentioned, the inclusions present in the clear quartz are less deformed than the ones present in the cloudy quartz (**Q1b**). This partition of inclusions suggests that the clear quartz is a later stage of overgrowth (part of **Q1c** or final stage of **Q1b**) on the earlier cloudy quartz (**Q1b**). This clear quartz overgrowth stage (**Q1c**) is characterised by a consistent low-saline, aqueous, H_2O-NaCl, fluid composition (**F2**), which also occur as secondary inclusions within **Q1**, while the cloudy, earlier quartz stage (**Q1b**) is characterized by a variable aqueous-gaseous composition (**F1**).

5.2. Raman microspectroscopy

Raman microspectroscopy has been performed on the same samples analyzed with fluid inclusion microthermometry, determining the volatile content of the aqueous-gaseous fluid inclusions. A Bruker-Senterra Nd confocal laser spectrometer, connected to an Olympus BX50 optical microscope (Royal Belgian Institute of Natural Sciences) has been used. Measurements were made with 20 mW, a laser wavelength of 532 nm and a 100x lens. The measured spectrum is 114 to 4400 cm^{-1}. Measurements were calibrated with a NIST SRM2242 glass standard. The spectra were analyzed using the FISpec software.

The results of the Raman microspectroscopy reveal, on the one hand, that a clear mixing trend exists between a CO_2-rich and a N_2-rich end member composition for the **F1** type fluid (Fig. 12). CH_4 is relatively absent in the **F1** type fluid. The volatile
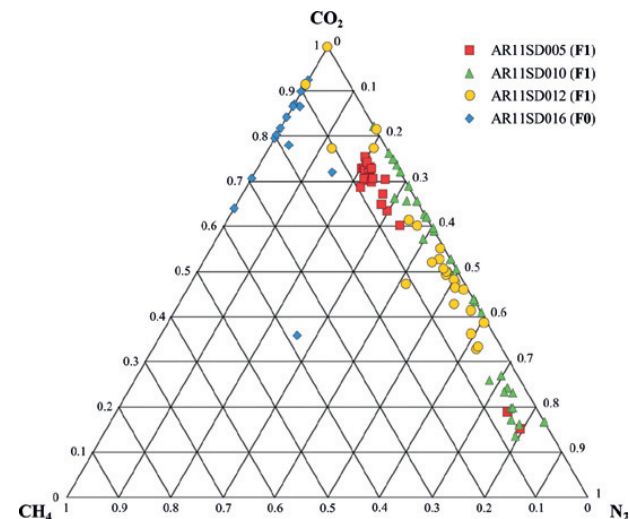
Figure 12: Ternary plot of the results of the Raman microspectroscopy. While the **F1** type fluids have a dominant CO_2-N_2 volatile composition, the **F0** type fluids show a dominant CO_2-CH_4 volatile composition.

composition of the aqueous-gaseous fluid encountered in the bedding-perpendicular, interboudin vein (**Q0** – *AR11SD016*), on the other hand, has a CO_2-CH_4 enriched volatile content and contains nearly no N_2 (Fig. 12). Hence, this composition does not match with the **F1** fluid type encountered at the MMQO (**Q1**) and in the cleavage-parallel veins (**Q2**), but should be defined as a new **F0** fluid type.

Combining the results of the Raman microspectroscopy with the results from the microthermometry, the following fluid inclusion types can be defined:

(**F0**) aqueous-gaseous fluid inclusions (H_2O-CO_2-CH_4-NaCl), encountered in the bedding-normal, interboudin veins (**Q0** – *AR11SD016*);

(**F1**) aqueous-gaseous inclusions (H_2O-CO_2-N_2-NaCl), encountered in the cloudy, quartz matrix of the main site (**Q1b** – *AR11SD005*, *AR11SD010*) and within the cleavage-parallel veins (**Q2a** – *AR11SD012*);

(**F2**) aqueous inclusions (H_2O-NaCl), with a salinity that ranges from 0.3 to 9.9 eq. NaCl wt% NaCl. These fluids were encountered in samples *AR11SD001*, *AR11SD005* and *AR11SD012*, within the clear quartz of stages **Q1c** and **Q2b**, but never in the cloudy quartz matrix. The inclusions show homogenization temperatures from 125 to 190 °C. The **F2** type inclusions that were analyzed with Raman microspectroscopy did not show any detectable amount of gases.

6. Chlorite geothermometry

Chlorites from 7 samples of **Q2** quartz were measured on a Jeol JXA8530F Field Emission Electron Probe Microanalyser (KU Leuven, MTM department) run at 15 kV and 15 nA. Samples were coated with a 5 nm thick Pt/Pd layer with the Quorum Q150TS coating device, to avoid surface charging. Different crystals were selected from each sample containing chlorites, depending on the quantity and quality of the chlorites present. Depending on the size of these crystals, between 3 and 6 WDS (wavelength dispersive spectroscopy) spot measurements were made. The intensity of the outgoing beam per unit wavelength is measured by a TAPH crystal for Mg and Al, a TAP crystal for O, a LIFH crystal for Mn, Fe and Cr, a LIF crystal for Ti and Ni and a PETH crystal for Si. Periclase was chosen as standard for O and Mg. Obsidian, willemite, hematite, pyrope, yttrium aluminium garnet, benitoite and nickel silicide were chosen as standards for Si, Mn, Fe, Cr, Al, Ti and Ni respectively.

Based on the Si-content versus the Fe/(Fe+Mg)-ratio (Hey, 1954) broadly two types of chlorites can be distinguished (Fig. 13). The largest group lies in the ripidolite – brunsvigite/pycnochlorite fields, while the other group lies predominantly in the diabantite field. Both types occur in each sample.

Temperatures were calculated according to different models. Three of these are based on empirical formulae (Cathelineau, 1988; Hillier & Velde, 1991; Jowett, 1991) and one is based on a solid solution thermodynamic model (Walshe, 1986). The calculated temperatures indicate that of the empirical models, the equations of Cathelineau (1988) and Jowett (1991) yield higher values than the Hillier & Velde (1991) equation. In general, the equation of Hillier & Velde (1991) and the model of Walshe (1986) at 100 MPa yield similar values of ca. 235 °C. The Walshe (1986) equation shows a much narrower range than the Hillier & Velde (1991) equation. These observations are similar to other studies comparing the different chlorite geothermometers (de Caritat et al., 1993; Inoue et al., 2009, 2010; Zhang et al., 1997).

The calculated temperatures, based both on empirical equations and on thermodynamic models, show a large range within one sample even after excluding low-quality measurements. Because

the chlorites and the quartz matrix (**Q1b**) from the MMQO (**Q1**) precipitated at different stages in the paragenesis (see paragraph 7.1), a direct correlation between temperatures obtained from chlorite from cleavage-parallel quartz veins (**Q2**) and temperature conditions at the MMQO (**Q1**) is, at best, contentious. Comparison within the **Q2** generation is not possible because of the unreliable microthermometric measurements for sample *AR11SD012*. The large range indicates that the composition of the chlorites was not predominantly determined by temperature but also by other factors such as pressure, bulk rock composition, fluid composition and by rate of mineral growth (Walshe, 1986; de Caritat et al., 1993). Therefore, it was not possible to use the temperature obtained as an independent geothermometer for precipitation conditions.

7. Discussion

7.1. Synthesis of vein generations and associated fluid stages

A total of three main quartz-vein generations have been recognized in the Mousny area. Besides quartz, also chlorite, muscovite, metal-bearing minerals and carbonates can be found in the different vein generations (Fig. 14).

A first vein-quartz generation (**Q0**), encountered in synorogenic, interboudin veins (*AR11SD016*), is characterized by a mixed aqueous-gaseous fluid (**F0**) that has a predominant H_2O-CO_2-CH_4-NaCl composition. Total homogenization temperatures of 112 and 155 °C are observed. Since decrepitation occurred rapidly upon heating and the inclusions were very small (< 5 μm) and hence not all temperatures were measureable, no isochores have been calculated for these fluid inclusions.

A second vein-quartz generation (**Q1**) consists of the different stages of vein infill that were encountered in the MMQO (Fig. 14). A first quartz stage (**Q1a**) consists of thin veinlets, made up of elongate-blocky quartz crystals. These veinlets, found in the host-rock fragments in the MMQO, already crosscut the cleavage fabric within the host-rock fragments. Hence, the veinlets (and the MMQO in general) postdate cleavage formation in the HASB and should be considered as syn- to late-orogenic
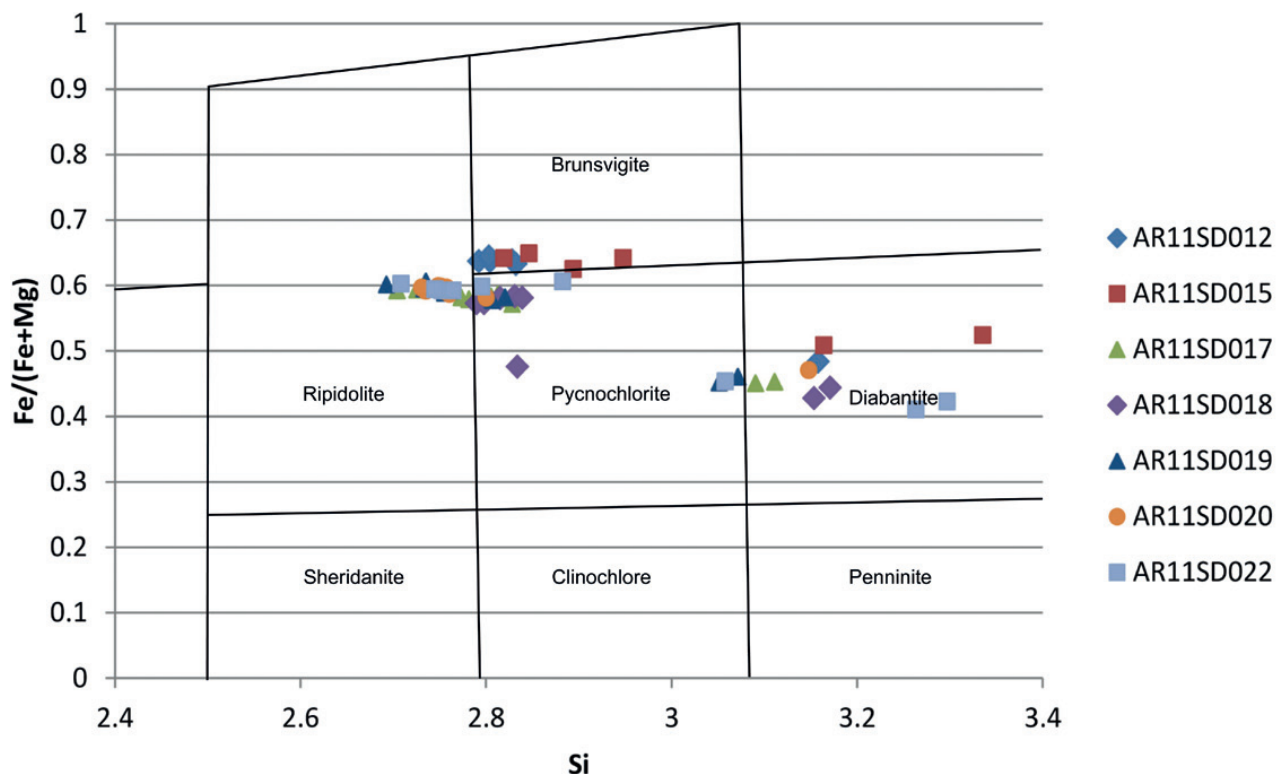

Figure 13: Plot of the Si-content versus the Fe-number with an overlay of the chlorite classification by Hey (1954). See Fig. 4 for sample location.

in nature (Fig. 14). The **Q1a** vein quartz shows a pink to bright blue luminescence under hot cathodoluminescence. The veinlets, in turn, are disrupted by the bulk, massive matrix quartz of the MMQO (**Q1b**).

Afterwards, a stage of chlorite formation occurred in between cleavage planes, primarily based on the exclusive occurrence of chlorite at the vein walls. During this chlorite stage, or shortly afterwards, the bulk quartz of the MMQO (**Q1b**) precipitated (Fig. 14). During this second quartz stage, muscovite grew. Muscovite is indeed found within the **Q1b** and **Q2a** quartz (Fig. 9D-E). The muscovite stage most probably predates the **Q1c** and **Q2b** clear quartz infill, primarily because of their absence within the latter quartz infill. The **Q1b** quartz is characterized by a dusty appearance, several deformation microstructures and predominantly blue luminescence colours under hot cathodoluminescence. Although optical microscopy shows signs of crystal-plastic deformation, the cathodoluminescence microscopy shows also signs of brittle deformation affecting "precursor" crystals and growth zones. Cathodoluminescence microscopy indeed shows that the **Q1b** stage can be further subdivided into minimum four growth stages (Fig. 14): "precursor" crystals with growth zones yielding a bright blue to yellowish luminescence (**A**), overprinting of this stage causing a darker blue luminescence (**B**), a fracturing stage affecting the "precursor" crystals, with infill of the created space with dark blue luminescent quartz (**C**), and a second fracturing stage further affecting the quartz mass with a second infill of the newly created space also with dark blue luminescent quartz (**D**). These last two stages of infill probably also caused the formation of the dark blue luminescent quartz matrix making up the bulk of the **Q1b** quartz.

A mixed aqueous-gaseous fluid (**F1**), with a variable H_2O-CO_2-N_2-NaCl composition, was encountered in quartz samples from both the MMQO (**Q1b**) (*AR11SD005* and *AR11SD010*) and the cleavage-parallel veins (**Q2a**) (*AR11SD012*) (Fig. 14). Besides the compositional similarities with the cleavage-parallel veins, the observed deformation microstructures correspond well between the MMQO and the cleavage-parallel veins. The microstructures (e.g. bulging recrystallization) indicate deformation conditions at relatively low temperatures (200 to 400 °C) and high strain rates (cf. Passchier & Trouw, 2005). The similarity in composition and crystal-plastic deformation strongly supports the hypothesis that the MMQO is kinematically intimately related and cogenetic to the cleavage-parallel veining in the area (Fig. 14).
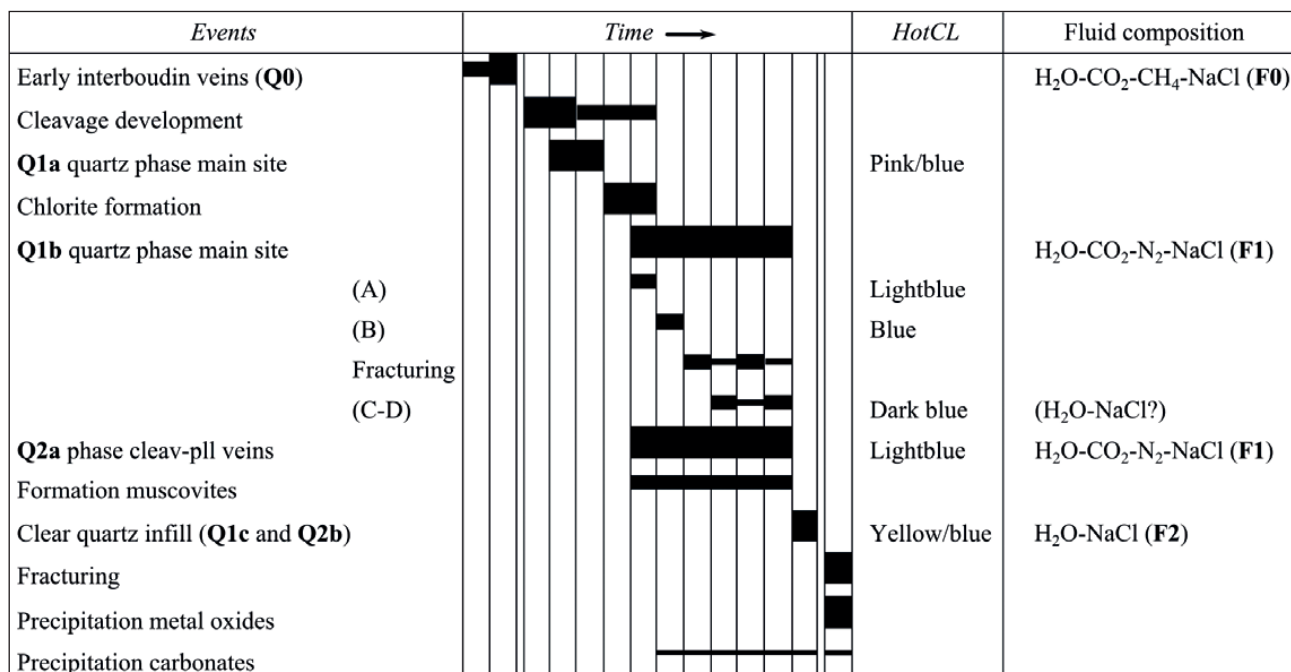
The entire **F1** fluid phase is characterized by a H_2O-CO_2-N_2-NaCl mixed aqueous-gaseous fluid composition. The fluid inclusions from the different analyzed samples display variable vapour-liquid ratios and differences in their cooling and heating behaviour, indicating a significant degree of deformation and leaking of the inclusions in *AR11SD005* and *AR11SD012*. The *AR11SD010* are the only reliable inclusions showing relatively narrow ranges in their vapour-liquid ratio, Thtot, ThCO2 and their salinity (Fig. 11). The mixed aqueous-gaseous inclusions of *AR11SD010* are characterized by lower homogenization temperatures (ca. 275 °C) compared to the temperatures measured for the deformed inclusions of *AR11SD005* and *AR11SD012* (ca. 345 °C). A volatile mixing trend between CO_2- and N_2-enriched fluids is revealed by the Raman spectroscopy (Fig. 12). The occurrence of this mixing ratio indicates local variations in the contribution of gaseous components from organic matter and phyllosilicates in the metasedimentary host rocks (e.g. bastonite, a NH_4^+-rich phyllosilicate) (Darimont, 1986; Kenis et al., 2005).

After the main quartz stage, a final quartz stage occurred in both the MMQO (**Q1c**) and the cleavage-parallel veins (**Q2b**) (Fig. 14). This quartz stage is represented by the more transparent, clear quartz inside the milky quartz mass (**Q1b** and **Q2a**). **Q1c** and **Q2b** quartz is characterized by a bright blue to yellow colour under hot cathodoluminescence, and likely formed under different conditions compared to the main quartz mass. The clear quartz stage in both the MMQO and the cleavage-parallel veins is characterized by an aqueous fluid (**F2**) with a H_2O-NaCl composition (Fig. 14). The measured fluid inclusions show lower, well-defined homogenization temperatures (ca. 120-180 °C) and the salinities range from 0.3 to 9.9 eq. NaCl wt%.

Lastly, a fracturing event took place, in which metal oxides precipitated in the cracks. At this time, or later, carbonates precipitated as well.

7.2. Comparison with regional fluid evolution

The observed fluid types in the Mousny area comply very well with the regional fluid evolution scheme of the epizonal HASB as defined by Kenis et al. (2005) (Fig. 15). The fluids indeed show a similar evolution from an early orogenic, mixed aqueous-gaseous metamorphic fluid (**F0**), enriched in CO_2 and CH_4 volatiles, to a later synorogenic, aqueous-gaseous metamorphic fluid (**F1**), enriched in CO_2 and N_2, and eventually to a late-orogenic aqueous H_2O-NaCl fluid (**F2**) (Fig. 15). The **F0** type fluid is very

Events	Time ⟶	HotCL	Fluid composition
Early interboudin veins (**Q0**)	▬		H_2O-CO_2-CH_4-NaCl (**F0**)
Cleavage development	▬		
Q1a quartz phase main site	▬	Pink/blue	
Chlorite formation			
Q1b quartz phase main site	▬▬		H_2O-CO_2-N_2-NaCl (**F1**)
(A)	▬	Lightblue	
(B)	▬	Blue	
Fracturing	▬		
(C-D)	▬	Dark blue	(H_2O-NaCl?)
Q2a phase cleav-pll veins	▬▬	Lightblue	H_2O-CO_2-N_2-NaCl (**F1**)
Formation muscovites	▬		
Clear quartz infill (**Q1c** and **Q2b**)	▬	Yellow/blue	H_2O-NaCl (**F2**)
Fracturing	▬		
Precipitation metal oxides	▬		
Precipitation carbonates			

Figure 14: Relative timing of veining and associated events, assembling observations and results from field relationships, optical microscopy, hot cathodoluminescence, fluid inclusion microthermometry and Raman microspectroscopy.

similar to the **A1** type fluid of Kenis et al. (2005), typical for the pre-orogenic, late burial fluids in the Ardenne-Eifel basin (Fig. 15). However, because of the structural evidence indicative of a synorogenic origin of the **Q0** quartz, it is fair to assume that the **F0** type fluid most likely represents a more-evolved synorogenic fluid of the original burial-related **A1** type fluid. The subsequent evolution from the **F0** type fluid in the synorogenic, interboudin veins (**Q0**) to the **F1** type fluid in the late-orogenic MMQO (**Q1**) and cleavage-parallel veins (**Q2**) complies with the general increase of the N_2 component during orogeny, as observed in the evolution from the gaseous CO_2-N_2-CH_4 (**A2**) to the gaseous N_2-(CH_4) fluid (**G1**) at Bertrix (Kenis et al., 2005) (Fig. 15). This increase in N_2 is related to the progressive release of nitrogen bound on organic material and/or maturation of the silicate host rock during progressive metamorphism (Darimont et al, 1988; Kenis et al., 2005). In the epizonal part of the slate belt, the salinity for earliest (**A1**) and latest fluid generations (**W1**) varies between 0.6 and 17 eq. NaCl wt%, and 3 and 10.6 eq. NaCl wt%, respectively (Kenis et al, 2005). These salinity ranges agree relatively well with the salinities observed for the **F1** and the **F2** type fluids, i.e. 4.5 to 6 eq. NaCl wt% (for the reliable *AR11SD010* **F1** inclusions) and, 0.3 to 9.9 eq. NaCl wt%, respectively. In this respect the late-orogenic **F2** type fluid correlates very well with the **W1** type fluid of Kenis et al. (2005), observed both in the anchizonal and epizonal part of the HASB.

Moreover, the particular metamorphic fluid composition exclude any link with the post-tectonic, Mesozoic, mostly Mississippi Valley-type Zn-Pb deposits characterized by a H_2O-$NaCl$-$CaCl_2$ composition (Dewaele et al., 2004; Muchez et al., 2005; Piessens et al., 2002).
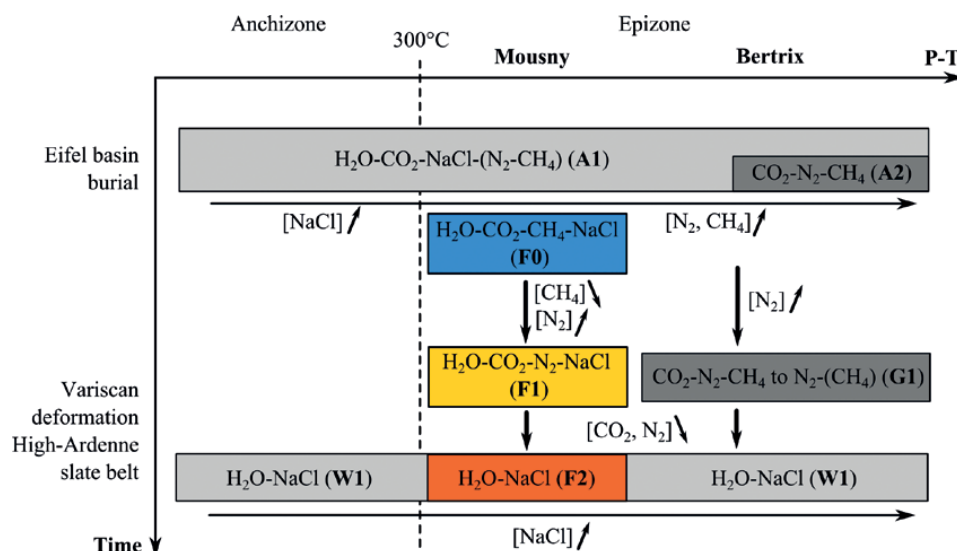
7.3. P-T conditions veining

In order to estimate the trapping conditions of the different fluid phases, isochores are constructed for the different FIAs. Integrating the results from fluid inclusion microthermometry and Raman microspectroscopy into the software package (Density, Ice, Clathrate) by Bakker (1997), and correlating them with the equations of state by Darling (1991) and Diamond (1992), the composition of the mixed aqueous-gaseous inclusions is further defined. The results of these calculations are further integrated in the Bulk and ISOC software packages (Bakker, 2003), which eventually yield the fluid isochores in question. Hence, we obtain three sets of isochores: (1) the **F1** type fluid (*AR11SD010*) with a density ranging between 0.91 and 0.92 g/cm³, (2) a second set for the **F1** type fluid (*AR11SD010*) with a density ranging between 0.77 and 0.85 g/cm³, and (3) the **F2** type fluid with a density ranging between 0.91 and 0.97 g/cm³ (Fig. 16). Isochores for the other fluid phases could not be calculated due to a lack of data.

To retrieve the original trapping conditions of the fluids, geothermal gradients are used (cf. Van Noten et al., 2011). Independent geothermometers and geobarometers, but also intersecting isochores of cogenetic fluids, are lacking. Several independent metamorphic criteria, however, can be taken into account to constrain the P-T conditions of veining. Metamorphism in the HASB is known to have a dominant burial, pre- to early synorogenic origin (Fielitz and Mansy, 1999), ranging from epizonal metamorphism in the deepest parts of the Ardenne-Eifel basin to anchizonal in the periphery of the basin (Fielitz and Mansy, 1999; Mosar, 1987). Based on the location of the study area in the epizonal part of the basin (Fielitz and Mansy, 1999), a peak metamorphic temperature of ca. 350 °C is proposed for the analyzed rocks (Fig. 16). In the central part of the HASB, metamorphic temperatures of 300-400 °C have indeed been inferred based on the metamorphic mineralogy (Beugnies, 1986; Theye & Fransolet, 1993), fluid inclusions (Darimont et al., 1988) and chlorite geothermometry (Verhaert, 2001). All vein quartz studied show a similar degree of crystal-plastic deformation, indicative of low- to moderate-temperature, crystal-plastic deformation between 200 and 400 °C (Passchier & Trouw, 2005), which suggests that quartz precipitation occurred at mid-crustal levels prior to the end of Variscan deformation. The predominant deformation mechanism, i.e. bulging recrystallization, indicates that deformation took place at relative high strain rates in brittle-plastic transitional settings. This mid-crustal depth level for the HASB has been inferred by Kenis et al. (2002) at a maximum burial depth of ca. 10 km (i.e. ca. 265 MPa) for the central HASB (Fig. 16).

Fluid inclusion data (Darimont, 1986), mineral assemblages (Beugnies, 1986), and conodont alteration indices (Helsen, 1995) all indicate a high geothermal gradient of ca. 50 °C/km for prograde, burial history of the Ardenne-Eifel basin. The study of fracture-filling zeolites, prehnite and pumpelllyite in the area of Bertrix, however, has inferred a retrograde geothermal gradient of ca. 35 °C/km for the retrograde, late- to postorogenic stage of the Variscan orogeny (Hatert and Theye, 2005). Taking into account the kinematic constraints of the development of the MMQO post-dating cleavage development and chlorite formation (Fig. 13), it is fair to assume that the MMQO originated on the retrograde path (cf. Jacques et al., 2014a). We therefore use a geothermal gradient of ca. 35 °C/km, for lithostatic and hydrostatic pressures, to further constrain the P-T trapping conditions of the different fluid stages (Fig. 16).

It is obvious that the two isochore sets for the same **F1** type fluid do not represent identical physical and chemical conditions of the FIA at the time of trapping (e.g. Bodnar, 2003). The isochore sets show a strong variation in density, with a range from 0.77 to 0.92 g/cm³, and record a strongly different internal fluid pressure upon homogenization, with values of 135 and 10 MPa

Figure 15: Graphical representation of the regional fluid evolution in the anchizonal and epizonal part of the HASB (after Kenis et al., 2005), combined with the fluid types encountered in the vein quartz in and around the MMQO. A comparison between both reveals that the fluid evolution within the MMQO bears a strong resemblance to the regional fluid evolution in the epizonal core of the HASB, from early, burial-related, metamorphic fluids (blue; **F0**), to early- and synorogenic fluids (yellow; **F1**) and eventually late- to post-orogenic fluids (orange; **F2**).

Figure 16: P-T-diagram illustrating the trapping conditions for both the **F1** and **F2** type fluids. Both the minimum and maximum isochores, for the respective m i c r o t h e r m o m e t r i c measurements, are represented for all fluid types. Also the isochores of the stretched **F1** type fluid inclusions are indicated (in orange). The inferred maximum metamorphic temperature (ca. 350 °C) is marked, as well as the maximum burial depth (ca. 10 km). Both the lithostatic and hydrostatic retrograde, geothermal gradient of 35 °C/ km are indicated. The ranges of the suggested trapping conditions for both the **F1** and **F2** type fluids are indicated by the red and blue filling, respectively.
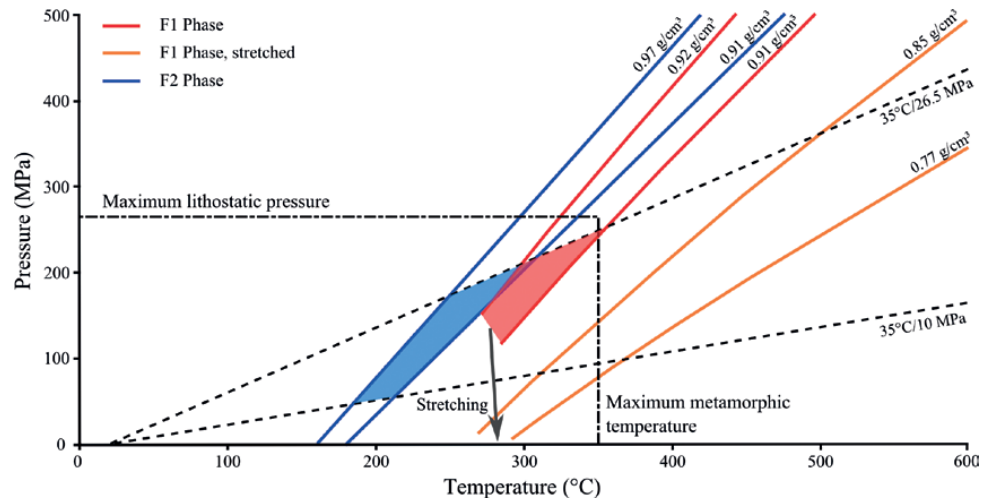
for set (1) and (2), respectively (Fig. 16). From the composition of the inclusions in question it is obvious that the isochores of set (2), with low densities from 0.77 to 0.85 g/cm³, represent stretching of the original fluid inclusion assemblage, which in turn is represented by isochore set (1). In accordance with the variation in fluid density, a similar H_2O-fraction (ca. 0.93 to 0.94%) and salinity (4.4 to 4.9 eq. NaCl wt% NaCl) for both isochore sets confirm stretching of isochore set (2). Stretching leads to a volume increase of the inclusion, causing an internal drop in pressure and density, while the composition remained identical (e.g. Goldstein, 2001). Only a minor increase (ca. 10 to 20 °C) in Thtot occurred. The latter isochores will therefore not be used in the following reconstruction of the P-T path.

Hence, the P-T conditions can only be deduced for isochore sets (1) and (3), from their intersection with the suggested geothermal gradients (Fig. 16). The resulting P-T ranges (red and blue boxes; Fig. 16) indicate that the **F1** and **F2** type fluids precipitated at 275-350 °C / 120-245 MPa, and 185-305 °C / 45-215 MPa, respectively. Because the HASB is a rock-buffered fluid system (Kenis et al., 2005), the P-T conditions measured for the fluid inclusions reflect the thermal history of the host rock along the retrograde metamorphic path. As such, the minor overlap between the fluid isochores (Fig. 16) suggests a relative timing for both fluids. The fluids precipitated in successive steps along the retrograde deformation path, with the H_2O-NaCl fluid (**F2**) precipitating at lower temperatures and pressures than the mixed aqueous-gaseous, H_2O-CO_2-N_2-NaCl fluid (**F1**). These results confirm the diachronuous pre- to synorogenic (**F1**) and late- to postorogenic (**F2**) nature of these fluids, as already suggested by Kenis et al. (2005) (Fig. 15).

Furthermore, these microthermometric results on the relative timing of the different fluids corroborate the observations from vein petrography. The relatively clear quartz zones (**Q1c** and **Q2b**) incorporating H_2O-NaCl fluid inclusions (**F2**), indicate a considerably smaller degree of crystal-plastic deformation. This smaller degree of crystal-plastic deformation is explained by the late-orogenic precipitation of **F2** type fluids during the waning stages of the Variscan orogeny, characterized by considerably lower P-T conditions. In a similar manner, a relative timing for the mixed aqueous-gaseous fluids (**F1**) of samples *AR11SD005* and *AR11SD010* can be suggested. Petrography of thin sections and wafers indicate that the low-density **F1** type fluid inclusions from *AR11SD010* occur in generally less-strained quartz than the inclusions from *AR11SD005*. Hot cathodoluminescence also indicates that the cloudy quartz from sample *AR11SD010* displayed a more or less homogeneous, dark blue luminescence, while the same quartz from sample *AR11SD005* shows variations in luminescence. Both of these features suggest that the quartz from sample *AR11SD005* precipitated under slightly different

physical and chemical conditions than the quartz of sample *AR11SD010*.

7.4. Mousny massive quartz occurrence, a dilational jog?

The elongated host-rock fragments in the MMQO, and their internal cleavage, oriented subparallel to the regional cleavage attitude (Fig. 6C), as well as the similar evolution in both the milky vein quartz in the cleavage-parallel veins (**Q2**) and the MMQO (**Q1**), strongly argues that the MMQO is kinematically intimately related to the formation of the cleavage-parallel veins. We therefore assume that the MMQO is a particular type of the cleavage-parallel veins. The temporal relationship of the cleavage development and the occurrence of N_2-enriched mixed aqueous-gaseous fluid inclusions (**F1**) within both the MMQO and the cleavage-parallel veins, moreover suggest that the veining occurred late in the Variscan orogeny (Fig. 15). In this respect, the cleavage-parallel veins in the Mousny area (**Q2**), and thus also the MMQO (**Q1**), may very well correlate with the discordant veins (**DV**) in the Herbeumont area (Fig. 1), which contain similar aqueous-gaseous H_2O-CO_2-N_2-NaCl fluid inclusions in growth zones (Van Baelen, 2010).

Considering the parallel to near-parallel orientation of the **Q2** quartz veins with respect to the slaty cleavage anisotropy, it can be argued that the cleavage planes were activated as mode I extensional fractures, in which quartz could subsequently precipitated. Mode I fracturing would imply that the minimum effective principal stress (s_3) should be near-perpendicular to the cleavage attitude (cf. Cox, 2005).

With respect to the orientation of the maximum effective principal stress (σ_1), two alternative scenarios should be considered: (1) a scenario in which the maximum effective principal stress (σ_1) is parallel to the dip direction of the cleavage anisotropy (Fig. 17A), and (2) a scenario in which the maximum effective principal stress (σ_1) is parallel to the strike of the cleavage anisotropy (Fig. 17B). The first scenario would imply an extensional stress regime, while the second scenario would imply a wrench stress regime.

In the wrench scenario, a subhorizontal maximum effective principal stress (σ_1) should thus be oriented ENE-WSW (Fig. 17B), which at first seems rather atypical within the overall geodynamic setting of the Variscan deformation in the HASB (Fig. 3) (Van Noten et al., 2012). However, such an anomalous stress state could be considered locally in the kinematic context of the NNE-SSW trending "Ourthe Zone" (Hance et al., 1999; Meilliez et al., 1991; Szaniawski et al., 2003). An ENE-WSW oriented maximum effective principal stress (σ_1) would indeed comply with the inferred dextral strike-slip on the NNE-SSW trending faults of the "Ourthe Zone" (Dejonghe, 2008) (Fig. 3B)
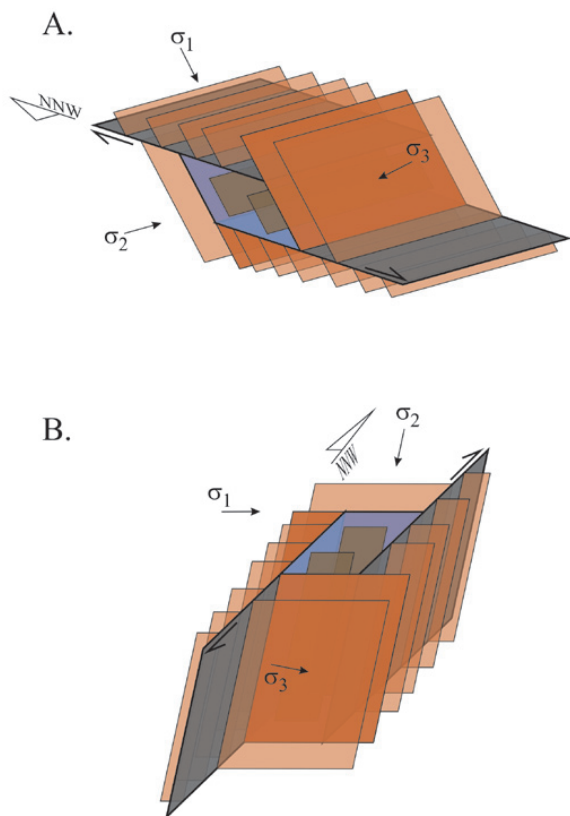
Figure 17: 3D conceptual sketch of a **dip-slip related dilational jog** (A) and a **strike-slip related dilational jog** (B), with the associated principal stress orientations. Cleavage planes in brown. Fault plane in dark grey. Dilational jog with cleavage-parallel host-rock fragments in grey-blue.

On the other hand, Van Noten et al. (2012) demonstrated in a theoretical 3D stress-state reconstruction that during tectonic inversions a transitional wrench stress regime should occur. To date, no structures have been described in literature that could possibly be linked to this transitional stage in the progressive deformation during tectonic inversion. In the wrench scenario, both the MMQO, as well as the cleavage-parallel quartz veins, may possibly be a candidate for such transitional structures, theoretically inferred by Van Noten et al. (2012).

In the extensional scenario, a near-vertical maximum effective principal stress (σ_1), trending NNW-SSE, is inferred (Fig. 17A). Considering the inferred similarity with the discordant veins in the Herbeumont area that evolved from initial, mode I parental fractures

at a small angle to the pre-existing cleavage in an extensional context with the maximum effective principal stress (σ_1) parallel to the dip direction of the cleavage (Van Baelen, 2010), as well as the strongly argued genetic relationship between the massive quartz occurrence and the cleavage-parallel veins, we favour the extensional scenario with the maximum effective principal stress (σ_1) oriented nearly parallel to the dip direction of the cleavage anisotropy, and subsequently the intermediate effective principal stress (σ_2) parallel to the strike of the cleavage anisotropy (Fig. 17A). Also the widespread occurrence of cleavage-parallel veins throughout the HASB, suggests no particular spatial link with the inferred "Ourthe Zone". This inferred extensional stress regime characterizes the late-orogenic extensional destabilization of the slate belt (e.g. Van Baelen, 2010) (Fig. 1), postdating a period of tectonic inversion. Van Noten et al. (2011, 2012) has demonstrated that these periods of tectonic inversion, both at the onset of orogeny (i.e. positive tectonic inversion) and in the late stages of orogeny (i.e. negative tectonic inversion), are periods of enhanced structural permeability, primarily due to the presence of high – up to (supra-)lithostatic – fluid pressures and low differential stresses (Fig. 1). This transient enhanced structural permeability is reflected in the widespread occurrence of tectonic inversion-related quartz veins within the HASB. Therefore, it is fair to assume that the **Q1** and **Q2** generations in both the MMQO and the cleavage-parallel veins, are related with the late-orogenic, negative tectonic inversion (Fig. 1).

We thus suggest that the MMQO is an excessively grown cleavage-parallel vein (Fig. 18). The best geometrical context to explain this localized massive quartz occurrence, is a dilational jog (Figs 17 & 18). Such dilational jogs commonly develop in step-overs (Fig. 19A) or bends (Fig. 19B), linking segments in fault zones (Childs et al., 1996; Cox et al., 2001; Micklethwaite et al., 2010). Classically, dilation in such fault-related jogs, is associated with episodic fluid-pressure drops caused by seismic, high strain-rate, fault movements (i.e. "suction pumping"; Sibson, 1987), often resulting in implosion breccias of the host-rock and pre-existing precipitates (Muchez & Sintubin, 1998; Sibson, 2000). The host-rock inclusions within the MMQO, containing a cleavage fabric and cross-cut by the **Q1a** vein generation, however, have preserved their attitude parallel to the regional cleavage attitude. This rather infers a more controlled, episodic, low strain-rate, opening of expanding cleavage-parallel veins, eventually generating a massive quartz occurrence (Fig. 18). The development of such a massive quartz occurrence can therefore best be compared to the crack-seal opening process of a single vein (e.g. Bons et al., 2012; Ramsay, 1980). The opening of such a dilational jog rather reflects a brittle, small-displacement accommodation within a rather diffuse shear zone (Fig. 19C). While the opening of fault-related, dilational jogs is controlled by episodic fault movement ("suction pumping"; Sibson, 1987) (Fig. 19A & B), we suggest that an episodic, fluid-pressure controlled
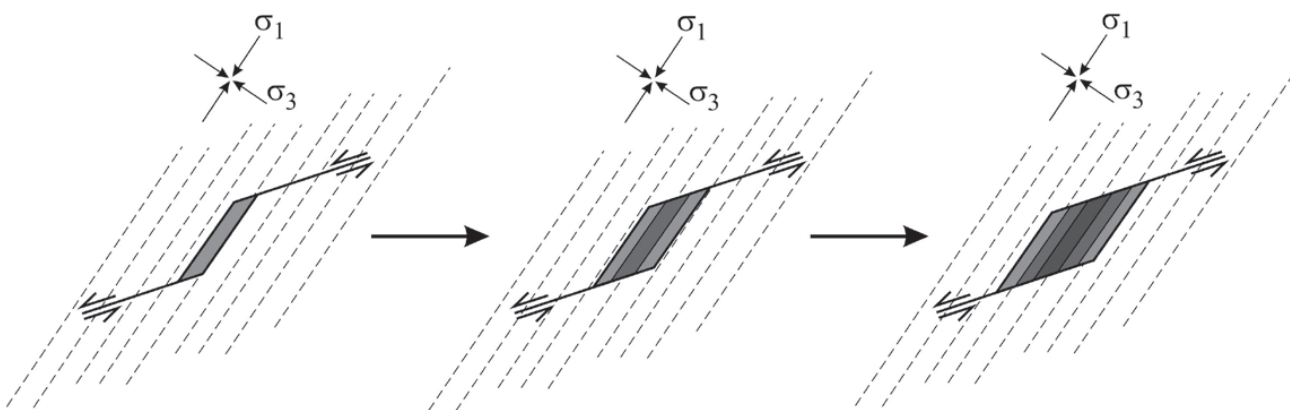
Figure 18: Model (cross-section) for the sequential opening of a cleavage-parallel vein, eventually resulting in a **dip-slip related dilational jog**, as represented by the MMQO, with host-rock inclusions preserving their original attitude parallel to the regional cleavage attitude (dashed lines).

opening of the cleavage-parallel dilation site controls the overall shear displacement (Fig. 19C).

It is fair to assume that throughout the slate belt a system of dilational jogs within a context of diffuse extensional shear zones (Fig. 19C), would develop during the extensional destabilization of the slate belt. In this respect, the Mousny-type dilational jog is considered very comparable to the discordant veins in the Herbeumont area (Van Baelen, 2010). The main difference is that the Mousny-type dilational jog reflects a purely brittle accommodation of the extensional shear localization, while the Herbeumont-type discordant veins reflect a mixed brittle-plastic shear accommodation, probably at a deeper structural level within the collapsing slate belt. Still, P-T conditions of the developing dilational jog at Mousny are such that low- to moderate crystal-plastic deformation, possibly related to the shear accommodation, is recorded in the quartz microfabric. Vein quartz occurrences in the wider Mousny area, as well as the cleavage-parallel veins, may very well be relics of other up-dip or down-dip dilational jogs in such a diffuse system (Fig. 19C). Similar massive quartz occurrences and rather thick cleavage-parallel milky quartz veins have indeed been reported by Dejonghe (2013). Finally, the widespread occurrence of large quartz boulders as decoration in gardens and as building material for chapels and houses all over the High Ardenne region, suggests that dilational jogs, as exposed at Mousny, may, very well be a rather common structural feature in the HASB.

8. Conclusions

When placing the MMQO into the different vein types of the HASB, i.e. (1) late burial bedding-normal veins, (2) early orogenic bedding-parallel veins, (3) synorogenic veins closely related to the development of folds and cleavage during the main contractional stage of the Variscan orogeny, and (4) late-orogenic discordant veins related to the orogenic collapse of the slate belt,

the MMQO seems to belong to the latest type. The attitude of the host-rock fragments within the MMQO, the cleavage-parallel veins in the area, the similar microstructures and fluid inclusion content in both, support this hypothesis.

Field observations of the host-rock fragments oriented according to the regional cleavage attitude, together with results from hot cathodoluminescence and microthermometry, can be fitted into a kinematic model of a dilational jog, creating a transient, high-permeability structure allowing significant fluid flow within the mid-crustal, low-permeability environment of a collapsing slate belt. The particular geometry of the dilational jog infers a gradual and constrained cycling of opening and sealing of voids with quartz, much like crack-seal veins instead of a "classical" suction-pump model.

All elements corroborate a model of a late-orogenic, extensional dilational jog to explain the MMQO, as well as similar occurrences throughout the HASB, and make it clearly favourable over the interpretation of the mineralized Mousny fault (Dejonghe 2008; Dejonghe & Hance, 2001). It also strengthens our proposition that the occurrence of massive vein quartz in the very poorly exposed parts of the HASB, should not be used as a proxy for the map trace of faults. It actually seems more probable that the majority of these massive quartz occurrences are a disperse phenomenon linked to the late-orogenic destabilization of the slate belt.

9. Acknowledgments
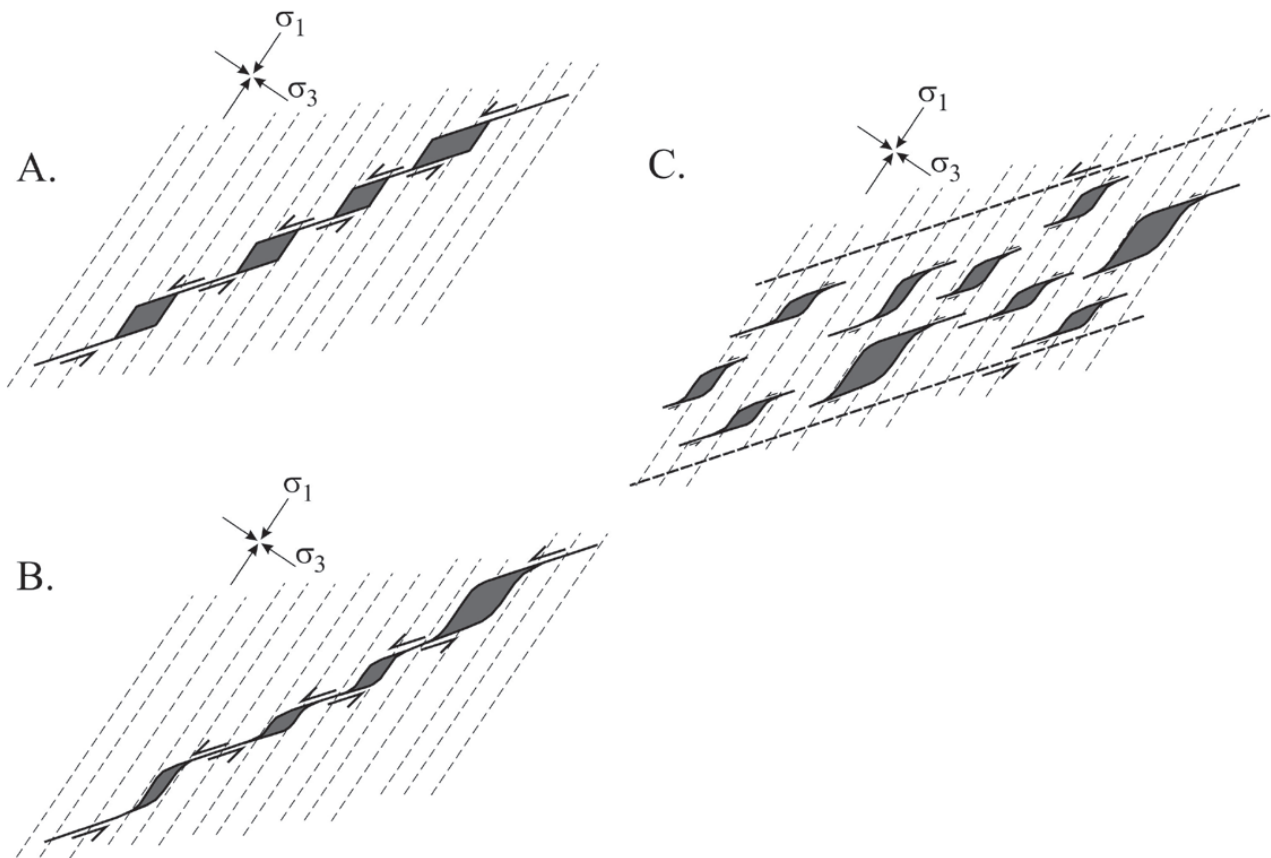
Figure 19: Different scenarios (cross-sections) of a low-angle, extensional detachment in which **dip-slip related dilational jogs**, as represented by the MMQO, can develop. (A) Dilational jogs in step-overs between fault segments. (B) Dilational jogs related to bends in the fault. (C) Disperse dilational jogs within a brittle-plastic shear zone. Cleavage is indicated by dashed lines. Principal stresses are indicated.

10. References

Bakker, R.J., 1997. Clathrates: Computer programs to calculate fluid inclusion V-X properties using clathrate melting temperatures. Computers & Geosciences, 23, 1-18.

Bakker, R.J., 2003. Package FLUIDS 1. Computer programs for analysis of fluid inclusion data and for modelling bulk fluid properties. Chemical Geology, 194, 3-23.

Becker, S.P., Eichhubl, P., Laubach, S.E., Reed, R.M., Lander, R.H. & Bodnar, R.J., 2010. A 48 m.y. history of fracture opening, temperature, and fluid pressure : cretaceous Travis Peak Formation, East Texas basin. Geological Society of American Bulletin, 122, 1081-1093.

Beugnies, A., 1986. Le métamorphisme de l'aire anticlinale de l'Ardenne. Hercynica, 2, 17-33.

Bodnar, R.J., 2003. Reequilibration of fluid inclusions. In: Samson, I., Anderson, A., Marshall, D. (Eds), Fluid Inclusions: Analysis and Interpretation. Mineralogical Association of Canada, Short Course, 213-231.

Boggs, S. & Krinsley, D., 2006. Application of Cathodoluminescence Imaging to the Study of Sedimentary Rocks. Cambridge University Press.

Boiron, M.-C., Cathelineau, M., Banks, D.A., Yardley, B.W.D., Noronha, F. & Miller, M.F., 1996. P-T-X conditions of late Hercynian fluid penetration and the origin of granite-hosted gold quartz veins in northwestern Iberia: A multidisciplinary study of fluid inclusions and their chemistry. Journal of Structural Geology, 60, 43-57.

Bons, P.D., Elburg, M.A. & Gomez-Rivas, E., 2012. A review of the formation of tectonic veins and their microstructures. Journal of Structural Geology, 43, 33-62.

Boullier, A.-M. & Robert, F., 1992. Palaeoseismic events recorded in Archaean gold-quartz vein networks, Val d'Or, Abitibi, Quebec, Canada. Journal of Structural Geology, 14, 161-179.

Bultynck, P. & Dejonghe, L., 2001. Devonian lithostratigraphic units. Geologica Belgica, 4, 39-69.

Cathelineau, M., 1988. Cation site occupancy in chlorites and illites as function of temperature. Clay minerals, 23, 471-485.

Cathelineau, M., Boiron, M.-C., Essarraj, S., Dubessy, J., Lespinasse, M. & Poty, B., 1993. Fluid pressure variations in relation to multistage deformation and uplift: a fluid inclusion study of Au quartz veins. European Journal of Mineralogy, 5, 107-121.

Childs, C., Nicol, A., Walsh, J.J. & Watterson, J., 1996. Growth of vertically segmented normal faults. Journal of Structural Geology, 18, 1389-1397.

Cox, S.F., 2005. Coupling between deformation, fluid pressures, and fluid flow in oreproducing hydrothermal systems at depth in the crust. Economic Geology 100th Anniversary Volume, 39-75.

Cox, S.F., Knackstedt, M.A. & Braun, J., 2001. Principles of structural control on permeability and fluid flow in hydrothermal systems. Reviews in Economic Geology, 14, 1-24.

Darimont, A., 1986. Les inclusions fluides de quartz filoniens d'Ardenne. Annales de la Société géologique de Belgique, 109, 587-601.

Darimont, A., Burke, E. & Touret, J., 1988. Nitrogen-rich metamorphic fluids in Devonian metasediments from Bastogne, Belgium. Bulletin de Minéralogie, 111, 321-330.

Darling, R.S., 1991. An extended equation to calculate NaCl contents from final clathrate melting temperatures in H2O-CO2-NaCl fluid inclusions: Implications for P-T isochore location. Geochimica et Cosmochimica Acta, 55, 3869-3871.

de Caritat, P., Hutcheon, I. & Walshe, J., 1993. Chlorite geothermometry; a review. Clays and Clay Minerals, 41, 219-239.

de Ruette, A., 1972. La légende des Cailloux de Mousny. Ardenne et Famenne, 46, 79-129.

Dejonghe, L., 2008. Le couloir de décrochement dextre de l'ourthe dans l'axe Erezée - Saint-Hubert (Haute Ardenne, Belgique) et son implication sur le tracé des failles longitudinales. Geologica Belgica, 11/3-4, 151-165.

Dejonghe, L., 2013. Geology of the Ardenne Anticlinorium, in the Amberloup – La Roche-en-Ardenn – Houffalize sector. The faults of the La Roche Syncline and the overturned Taverneux Anticline. Geologica Belgica, 16/3, 196-205.

Dejonghe, L. & Hance, L., 2001. Champlon – La Roche-en-Ardenne. Notice explicative de la carte géologique de Wallonie, 60/1-2. Direction générale des Ressources naturelles et de l'Environnement, Namur.

Dewaele, S., Muchez, P. & Banks, D.A., 2004. Fluid evolution along multistage composite fault systems at the southern margin of the Lower Palaeozoic Anglo-Brabant fold belt, Belgium. Geofluids, 4, 341-356.

Diamond, L.W., 1992. Stability of CO2 clathrate hydrate + CO2 liquid + CO2 vapour + aqueous KCl-NaCl solutions: Experimental determination and application to salinity estimates of fluid inclusions. Geochimica et Cosmochimica Acta, 56, 273-280.

Dietrich, D. & Grant, P., 1985. Cathodoluminescence petrography of syntectonic quartz fibres. Journal of Structural Geology, 7, 541-553.

Essarraj, S., Boiron, M.-C., Cathelineau, M. & Fourcade, S., 2001. Multistage deformation of Au-quartz veins (Laurieras, French Massif Central): evidence for late gold introduction from microstructural, isotopic and fluid inclusion studies. Tectonophysics, 336, 79-99.

Evans, M.A., Bebout, G.E. & Brown, C.H., 2012. Changing fluid conditions during folding: an example from the central Appalachians. Tectonophysics, 576-577, 99-115.

Fielitz, W. & Mansy, J.-L., 1999. Pre- and synorogenic burial metamorphism in the Ardenne and neighbouring areas (Rhenohercynian zone, central European Variscides). Tectonophysics, 309, 227-256.

Goldstein, R.H., 2001. Fluid inclusions in sedimentary and diagenetic systems. Lithos, 55, 159-193.

Götte, T. & Richter, D.K., 2006. Cathodoluminescence characterization of quartz particles in mature arenites. Sedimentology, 53, 1347-1359.

Götze, J., 2012. Application of Cathodoluminescence Microscopy and Spectroscopy in Geosciences. Microscopy and Microanalysis, 18, 1270-1284.

Grohmann, C.H. & Campanha, G.A.C., 2010. OpenStereo: open source, cross-platform software for structural geology analysis. Presented at the AGU 2010 Fall Meeting, San Francisco, CA.

Hance, L., Ghysel, P., Laloux, M., Dejonghe, L. & Mansy, J.-L., 1999. Influence of a heterogeneous lithostructural layering on orogenic deformation of the Variscan Front Zone (eastern Belgium). Tectonophysics, 309, 161-177.

Hatert, F. & Theye, T., 2005. Zéolites, Prehnite, and Pumpellyite from Bertrix, Belgian Ardennes. Geologica Belgica, 8, 33-42.

Helsen, S., 1995. Burial history of Palaeozoic strata in Belgium as revealed by conodont colour alteration data and thickness distributions. Geologische Rundschau, 84, 738-747.

Hey, M., 1954. A new review of the chlorites. Mineralogical Magazine, 30, 277-292.

Hillier, S. & Velde, B., 1991. Octahedral occupancy and the chemical composition of diagenetic (low-temperature) chlorites. Clay Minerals, 26, 149-168.

Inoue, A., Kurokawa, K. & Hatta, T., 2010. Application of Chlorite Geothermometry to Hydrothermal Alteration in Toyoha Geothermal System, Southwestern Hokkaido, Japan. Resource Geology, 60, 52-70.

Inoue, A., Meunier, A., Patrier Mas, P., Rigault, C., Beaufort, D. & Vieillard, P., 2009. Application of chemical geothermometry to low-temperature trioctahedral chlorites. Clays and Clay Minerals, 57, 371-382.

Jacques, D., Derez, T., Muchez, P. & Sintubin, M., 2014a. Syn- to late-orogenic quartz veins marking a retrograde deformation path in a slate belt: Examples from the High-Ardenne slate belt (Belgium). Journal of Structural Geology, 58, 43-58.

Jacques, D., Derez, T., Muchez, P. & Sintubin, M., 2014b. Regional significance of non-cylindrical folding in the northwestern part of the High-Ardenne slate belt (Redu-Daverdisse, Belgium). Geologica Belgica, 17, 252-267.

Jowett, E., 1991. Fitting iron and magnesium into the hydrothermal chlorite geothermometer. Geological Association of Canada/Mineralogic Association of Canada/Social Economic Geology Joint Annual Meeting, Vol. 16.

Kenis, I., Muchez, P., Verhaert, G., Boyce, A. & Sintubin, M., 2005. Fluid evolution during burial and Variscan deformation in the Lower Devonian rocks of the High-Ardenne slate belt (Belgium): sources and causes of high-salinity and C–O–H–N fluids. Contributions to Mineralogy and Petrology, 150, 102-118.

Kenis, I., Sintubin, M., Muchez, P. & Burke, E., 2002. The "boudinage" question in the High-Ardenne slate belt (Belgium): a combined structural and fluid-inclusion approach. Tectonophysics, 348, 93-110.

Lacroix, B., Buatier, M., Labaume, P., Travé, A., Dubois, M., Charpentier, D., Ventalon, S. & Convert-Gaubier, D., 2011. Microtectonic and geochemical characterization of thrusting in a foreland basin: example of the South-Pyrenean orogenic wedge (Spain). Journal of Structural Geology, 33, 1359-1377.

Mansy, J.-L. & Lacquement, F., 2002. Le Paléozoïque du Nord de la France et de la Belgique. Géologues, Revue officielle de l'Union Française des Géologues, 133-134, 7-24.

Meilliez, F., André, L., Blieck, A., Fielitz, W., Goffette, O., Hance, L., Khatir, A., Mansy, J.-L., Overlau, P. & Verniers, J., 1991. Ardenne-Brabant. Sciences Géologiques Bulletin, 44, 3-29.

Meilliez, F. & Mansy, J.-L., 1990. Déformation pelliculaire différenciée dans une série lithologique hétérogène: le Dévono-Carbonifère de l'Ardenne. Bulletin de la Société géologique de France, 6, 177-188.

Micklethwaite, S., Sheldon, H.A. & Baker, T., 2010. Active fault and shear processes and their implications for mineral deposit formation and discovery. Journal of Structural Geology, 32, 151-165.

Mosar, J., 1987. Schistosité et métamorphisme hercyniens dans les Ardennes Luxembourgeoises. Sciences Géologiques Bulletin, 40, 231-243.

Muchez, P., Heijlen, W., Banks, D., Blundell, D., Boni, M. & Grandia, F., 2005. Extensional tectonics and the timing and formation of basin-hosted deposits in Europe. Ore Geology Reviews, 27, 241-267.

Muchez, P. & Sintubin, M., 1998. Contrasting origin of palaeofluids in a strike-slip fault system. Chemical Geology, 145, 105-114.

Murphy, P. & Roberts, S., 1997. Melting and nucleation behaviour of clathrates in multivolatile fluid inclusions: evidence of thermodynamic disequilibrium. Chemical Geology, 135, 1-20.

Oncken, O., von Winterfeld, C.H. & Dittmar, U., 1999. Accretion of a rifted passive margin: The Late Paleozoic Rhenohercynian fold and thrust belt (Middle European Variscides). Tectonics, 18, 75-91.

Pagel, M., Barbin, V., Blanc, P. & Ohnenstetter, D., 2000. Cathodoluminescence in Geoscience. Springer-Verlag, Berlin Heidelberg.

Passchier, C.W. & Trouw, R.A.J., 2005. Microtectonics. Springer-Verlag, Berlin Heidelberg.

Piessens, K., Muchez, P., Dewaele, S., Boyce, A., De Vos, W., Sintubin, M., Debacker, T.N., Burke, E. & Viaene, W., 2002. Fluid flow, alteration and polysulphide mineralisation associated with a low-angle reverse shear zone in the Lower Palaeozoic of the Anglo-Brabant fold belt, Belgium. Tectonophysics, 348, 73-92.

Potter, R.W., Clynne, M.A. & Brown, D.L., 1978. Freezing point depression of aqueous sodium chloride solutions. Economic Geology, 73, 284-285.

Ramsay, J.G., 1980. The crack-seal mechanism of rock deformation. Nature, 284, 135-139.

Roedder, E., 1984. Fluid Inclusions. Vol. 12 of Reviews in Mineralogy, Mineralogical Society of America.

Servaye, P., 1955. Carnet Géologique. Geological mapping excercise.

Sibson, R.H., 1987. Earthquake rupturing as a hydrothermal mineralising agent. Geology, 15, 701-704.

Sibson, R.H., 2000. Fluid involvement in normal faulting. Journal of Geodynamics, 29, 469-499.

Sibson, R.H., 2004. Controls on maximum fluid overpressure defining conditions for mesozonal mineralisation. Journal of Structural Geology, 26, 1127-1136.

Sintubin, M., Debacker, T.N. & Van Baelen, H., 2009. Early Palaeozoic orogenic events north of the Rheic suture (Brabant, Ardenne): A review. Comptes Rendus Geoscience, 341, 156-173.

Szaniawski, R., Lewandowski, M., Mansy, J.-L., Averbuch, O. & Lacquement, F., 2003. Synfolding remagnetiztion events in the French - Belgium Variscan thrust front as markers of the fold-and-thrust belt kinematics. Bulletin de la Société géologique de France, 174/5: 511-523.

Theye, T. & Fransolet, A.-M., 1993. Amphibolitfazielle Metamorphite im Rhenohercynikum der Ardennen. Beih. z. Eur. J. Mineral., 5, 255.

Upton, P., Craw, D., Yu, B. & Chen, Y.-G., 2011. Controls on fluid flow in transpressive orogens, Taiwan and New Zealand. Geological Society, London, Special Publications, 359, 249-265.

Van Baelen, H., 2010. Dynamics of a progressive vein development during the late-orogenic mixed brittle-ductile destabilisation of a slate belt. Examples of the High-Ardenne slate belt (Herbeumont, Belgium). Aardkundige Mededelingen, 24, Leuven University Press.

Van Baelen, H. & Sintubin, M., 2008. Kinematic consequences of an angular unconformity in simple shear: an example from the southern border of the Lower Palaeozoic Rocroi inlier (Naux, France). Bulletin de la Société géologique de France, 179, 73-87.

Van den Kerkhof, A.M. & Thiéry, R., 2001. Carbonic inclusions. Lithos, 55, 49-68.

Van Noten, K., Hilgers, C., Urai, J.L. & Sintubin, M., 2008. Late burial to early tectonic quartz veins in the periphery of the High-Ardenne slate belt (Rursee, North Eifel, Germany). Geologica Belgica, 11, 179-198.

Van Noten, K., Muchez, P. & Sintubin, M., 2011. Stress-state evolution of the brittle upper crust during compressional tectonic inversion as defined by successive quartz vein types (High-Ardenne slate belt, Germany). Journal of the Geological Society, London, 168, 407-422.

Van Noten, K. & Sintubin, M., 2010. Linear to non-linear relationship between vein spacing and layer thickness in centimetre- to decimetre-scale siliciclastic multilayers from the High-Ardenne slate belt (Belgium, Germany). Journal of Structural Geology, 32, 377-391.

Van Noten, K., Van Baelen, H. & Sintubin, M., 2012. The complexity of 3D stress-state changes during compressional tectonic inversion at the onset of orogeny. In: Healy, D., Butler, R.W.H., Shipton, Z., Sibson, R.H. (Eds), Faulting, Fracturing and Igneous Intrusion in the Earth's crust. Geological Society, London, Special Publications, 367, 51-69.

Verhaert, G., 2001. Kwartsaders en dubbelzijdige mullions in de Lochkoviaan metasedimenten in de Hoge-Ardennenleisteengordel (Groeve La Flêche, Bertrix, België). Unpublished Graduate Thesis, Katholieke Universiteit Leuven.

Walshe, J.L., 1986. A six-component chlorite solid solution model and the conditions of chlorite formation in hydrothermal and geothermal systems. Economic Geology, 81, 681-703.

Zhang, Y., Muchez, P. & Hein, U.F., 1997. Chlorite geothermometry and the temperature conditions at the Variscan thrust front in eastern Belgium. Geologie en Mijnbouw, 76, 267-270.